



Cambrian bimodal volcanism in the Lhasa Terrane, southern Tibet: Record of an early Paleozoic Andean-type magmatic arc in the Australian proto-Tethyan margin

Di-Cheng Zhu ^{a,*}, Zhi-Dan Zhao ^a, Yaoling Niu ^{b,c}, Yildirim Dilek ^{a,d}, Qing Wang ^a, Wen-Hua Ji ^e, Guo-Chen Dong ^a, Qing-Lin Sui ^a, Yong-Sheng Liu ^f, Hong-Lin Yuan ^g, Xuan-Xue Mo ^a

^a State Key Laboratory of Geological Processes and Mineral Resources, and School of Earth Science and Resources, China University of Geosciences, Beijing 100083, China

^b School of Earth Sciences, Lanzhou University, Lanzhou 730000, China

^c Department of Earth Sciences, Durham University, Durham DH1 3LE, UK

^d Department of Geology, Miami University, Oxford, OH 45056, USA

^e Xi'an Institute of Geology and Mineral Resource, China Geological Survey, Xi'an 710054, China

^f State Key Laboratory of Geological Processes and Mineral Resources, and Faculty of Earth Sciences, China University of Geosciences, Wuhan 430074, China

^g State Key Laboratory of Continental Dynamics, Department of Geology, Northwest University, Xi'an 710069, China

ARTICLE INFO

Article history:

Accepted 30 December 2011

Available online 8 January 2012

Editor: K. Mezger

Keywords:

Whole-rock geochemistry

Zircon U–Pb dating and Hf isotope

Petrogenesis

Cambrian bimodal metavolcanic rocks

Lhasa Terrane

Southern Tibet

ABSTRACT

This paper reports new zircon LA-ICP-MS U–Pb age and Hf-isotope, whole-rock major and trace element, and Sr–Nd isotope data from Cambrian metavolcanic rocks in the central Lhasa subterrane of southern Tibet. These rocks form a bimodal volcanic suite consisting mainly of silicic metavolcanic rocks with subordinate metabasalts. Five silicic metavolcanic samples dated at ca. 492 Ma and one metabasalt sample yielding a near-concordant ²⁰⁶Pb/²³⁸U age of 492 ± 4 Ma indicate that mafic and silicic eruptions were contemporaneous. The metabasalts are mostly high-K calc-alkaline, enriched in Th, U, and light rare earth elements (LREEs), and depleted in Nb, Ta, Ti, Zr, and Hf, geochemically resembling the Andean arc basalts. The silicic metavolcanic rocks are high-K calc-alkaline and low in Nb and Zr. The metabasaltic rocks have negative whole-rock $\epsilon_{\text{Nd}}(t)$ values (–4.7 to –3.5) and varying zircon $\epsilon_{\text{Hf}}(t)$ values (–0.7 to +7.5), differing significantly from those of the silicic metavolcanic rocks, which yield negative whole-rock $\epsilon_{\text{Nd}}(t)$ values of –8.4 to –7.2 and varying zircon $\epsilon_{\text{Hf}}(t)$ values (–13.9 to –4.6). The metabasaltic rocks are interpreted as resulting from partial melting of an enriched lithospheric mantle source that was metasomatized by subduction-related components, whereas the silicic metavolcanic rocks were derived from basaltic melt-induced anatexis of the ancient Lhasa basement with inherited mantle melt signatures. The Western Qiangtang–Amdo–Tethyan Himalaya situated in the Indian proto-Tethyan margin and the Lhasa and other possible microcontinents or terranes (e.g., Gongshan, Baoshan, Tengchong, Burma, and Sibumasu) paleogeographically located in the Australian proto-Tethyan margin represent an early Paleozoic Andean-type magmatic arc facing the proto-Tethyan Ocean. The emplacement of the bimodal volcanic rocks and the development of the Cambro–Ordovician angular unconformity in the central Lhasa subterrane can be attributed to slab break-off of the proto-Tethyan Ocean lithosphere following the collisional accretion of microcontinents or terranes located outboard of the magmatic arc (possibly Eastern Qiangtang and South China).

© 2012 Elsevier B.V. All rights reserved.

1. Introduction

The late Precambrian–early Paleozoic time window was an important period in the geological evolution of Gondwana, as this was the time of the assembly of various continental components within the Gondwana supercontinent and the subduction initiation along the Peri-Gondwana margin (cf. Meert, 2003; Collins and Pisarevsky, 2005; Cawood and Buchan, 2007; Cawood et al., 2007; Li et al.,

2008a, 2008b; Murphy et al., 2011). Previous studies have indicated that the final assembly of the eastern Gondwana occurred between ca. 570 and ca. 510 Ma (cf. Meert, 2003; Cawood and Buchan, 2007 for a synthesis), and the subduction along the Gondwanan proto-Pacific margin initiated from 580 to 550 Ma (cf. Cawood and Buchan, 2007). However, whether the Gondwanan proto-Tethyan margin was an active continental margin or not is debated. For example, the early Paleozoic granitoids (~530–470 Ma) widely emplaced in the Indian proto-Tethyan margin have been interpreted as relating to the final assembly of Gondwana (Baig et al., 1988; Gaetani and Garzanti, 1991; Meert and Van der Voo, 1997), the supercontinental breakup (Murphy and Nance, 1991), or crustal extension in a non-arc environment (Miller et al., 2001). The Cambro–Ordovician

* Corresponding author at: State Key Laboratory of Geological Processes and Mineral Resources, China University of Geosciences, 29# Xue-Yuan Road, Haidian District, Beijing 100083, China. Tel.: +86 10 8232 2094(O); fax: +86 10 8232 2094.

E-mail address: dchengzhu@163.com (D.-C. Zhu).

angular unconformity identified along the length of the Himalayan orogen has been generally interpreted as recording a regional orogenic event in the northern Indian continent (Garzanti et al., 1986; Yin and Harrison, 2000; Gehrels et al., 2003, 2006; Cawood et al., 2007; Zhang et al., 2008a), but Myrow et al. (2006) argue against this interpretation and point out that the nature of this unconformity remains an enigma. Cawood et al. (2007) argued for the presence of the North India Orogen during the Early Paleozoic (530–490 Ma) and interpreted the granitoids and angular unconformity as a result of an Andean-type orogenic activity related to subduction of the proto-Tethyan Ocean lithosphere beneath the Indian continent. Collectively, these discrepancies seem to have resulted from (1) the strong overprinting of the Cenozoic tectonothermal events on the Early Paleozoic metamorphism and deformation, (2) the rare occurrence of coeval mafic rocks that are sensitive to geodynamic processes, and (3) the absence of a record of coeval Andean-type orogenic events in the modern-day northern Australian margin.

The Lhasa Terrane in southern Tibetan Plateau (Fig. 1a) has generally been speculated to have been rifted from northern India in the late Paleozoic (cf. Sengör, 1987; Yin and Harrison, 2000; Pan et al.,

2004; Metcalfe, 2006, 2009). However, new geological and abundant detrital zircon data indicate that the Lhasa Terrane came from northern Australia and experienced late Precambrian–early Paleozoic evolution in a different paleogeographical setting from that of the Qiangtang–Greater India–Tethyan Himalaya system (Zhu et al., 2011a, 2012). Recently, Cambrian volcanic rocks (~501 Ma; Ji et al., 2009a; 492 Ma, this study) and Cambro–Ordovician angular unconformity (Li et al., 2010), which are comparable to tectonomagmatic events identified in the northern Indian margin, have also been documented in the central Lhasa subterrane (Fig. 1b). These new observations, together with a new understanding of the origin of the Lhasa Terrane, allowed us to explore the nature of the tectonomagmatic events in northern Australia during the early Paleozoic, which are still poorly understood (Hocking and Mory, 2006). In this paper, we report zircon U–Pb age and Hf isotope data, whole-rock major and trace element analyses, and Sr–Nd isotope data of the metavolcanic rocks from southeastern Nyima in the central Lhasa subterrane (Fig. 1c). These data reveal the presence of the ~492 Ma bimodal volcanic rocks that predate the development of the Cambro–Ordovician angular unconformity both in the central Lhasa subterrane and at

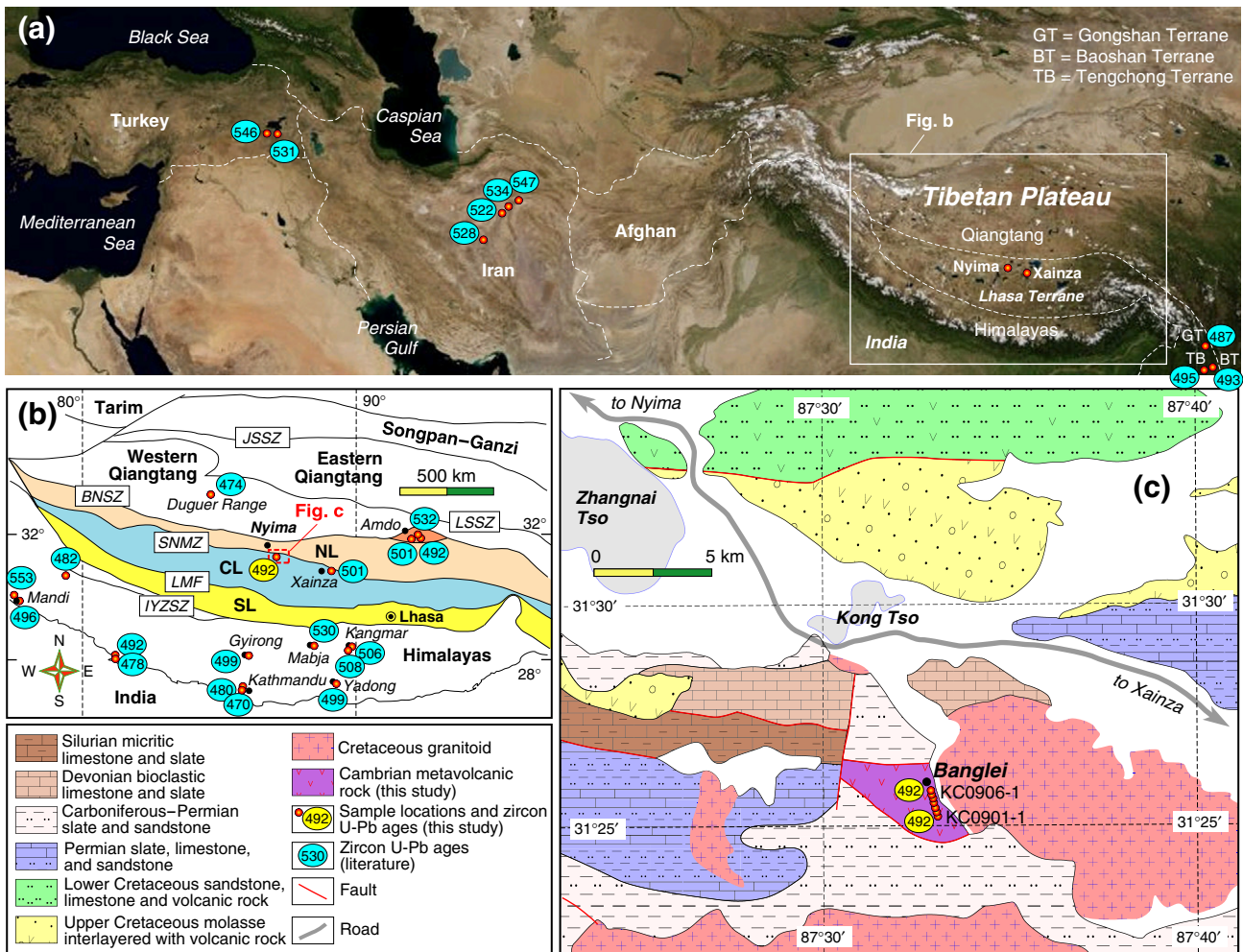


Fig. 1. (a) Geographic map of parts of Asia (<http://maps.nationalgeographic.com/maps>) showing the distributions of Early Paleozoic magmatic rocks in SE Turkey (Ustaömer et al., 2009), Central Iran (Ramezani and Tucker, 2003; Hassanzadeh et al., 2008), Gongshan (Song et al., 2007), Baoshan (Liu et al., 2009), and Tengchong (Chen et al., 2007). (b) Tectonic outline of the Tibetan Plateau showing the subdivision of the Lhasa Terrane (Zhu et al., 2012) and the distribution of Early Paleozoic magmatic rocks currently available. Data sources: Western Qiangtang (Pullen et al., 2011), Amdo (Xie et al., 2010; Guynn et al., 2012; our unpublished data); central Lhasa (Ji et al., 2009a; this study), Himalaya (cf. Miller et al., 2001; Cawood et al., 2007; Lee and Whitehouse, 2007; Quigley et al., 2008; Shi et al., 2010; Wang et al., 2011). JSSZ = Jinsha Suture Zone; LSSZ = Longmu Tso–Shuanghu Suture Zone; BNSZ = Bangong–Nujiang Suture Zone; SNMZ = Shiquan River–Nam Tso Mélange Zone; LMF = Luobadui–Milashan Fault; IYZSZ = Indus–Yarlung Zangbo Suture Zone. NL = Northern Lhasa subterrane; CL = Central Lhasa subterrane; SL = Southern Lhasa subterrane. (c) Geological map of the Banglei in SE Nyima in the central Lhasa subterrane (Lu et al., 2011), showing the location of the Banglei metavolcanic rocks investigated in this study.

the northern Indian margin. Our results, in combination with the known coeval magmatism and metamorphism, provide new insights into the petrogenesis and geodynamic processes responsible for the Early Paleozoic tectonomagmatic events along the India–Australia proto-Tethyan margin.

2. Geological background

From north to south, the Tibetan Plateau consists of the Songpan–Ganzi flysch complex, Eastern Qiangtang, Western Qiangtang, Lhasa Terrane, and the Himalayas (Fig. 1b). These terranes are separated by a series of suture zones, namely the Jinsha, Longmu Tso–Shuanghu, Bangong–Nujiang, and Indus–Yarlung Zangbo Suture Zones (Fig. 1b) (see Zhu et al., 2012). The Lhasa Terrane in southern Tibetan Plateau is divided into northern, central, and southern subterrane, separated by the Shiquan River–Nam Tso Mélange Zone and Luobadui–Milashan Fault (Fig. 1b).

The northern Lhasa subterrane has been interpreted to be underlain by a Cambrian or Neoproterozoic crystalline basement reported from the Amdo area (Amdo orthogneiss) (Xu et al., 1985; Dewey et al., 1988; Guynn et al., 2006), but recent studies have shown that the Amdo microcontinent is not an integral part of the Lhasa Terrane (Zhu et al., 2012). This subterrane is instead composed of juvenile crust (Zhu et al., 2011b) and is covered by Middle Triassic–Cretaceous sedimentary rocks with abundant early Cretaceous volcanic rocks and associated granitoids (cf. Pan et al., 2004; Zhu et al., 2012). The central Lhasa subterrane represents a microcontinent with Archean and Proterozoic basement rocks (Zhu et al., 2009a, 2011b, 2012). Recent studies have indicated that part of the Nyainqêntanglha Group in this subterrane has undergone multiple episodes of metamorphism during the Neoproterozoic (~720 Ma, Zhang et al., 2010; ~690 Ma, Dong et al., 2011a), Late Triassic (225–213 Ma, Dong et al., 2011b), and Cenozoic (Xu et al.,

1985; Kapp et al., 2005a). This reworked crystalline basement is covered by Permo–Carboniferous metasedimentary and Upper Jurassic–Lower Cretaceous sedimentary units with abundant volcanic rocks (Zhu et al., 2009a, 2011b, 2012), as well as minor Ordovician, Silurian, Devonian, and Triassic limestone occurrences (cf. Pan et al., 2004). The southern Lhasa subterrane is characterized by the existence of juvenile crust (cf. Mo et al., 2008; Ji et al., 2009b; Zhu et al., 2011b) with a Precambrian crystalline basement locally preserved (Zhu et al., 2012). This subterrane is dominated by the Cretaceous–Tertiary Gangdese Batholith and the Paleogene Linzizong volcanic succession (cf. Zhu et al., 2011b, 2012), with minor Triassic–Cretaceous volcano-sedimentary rocks that are largely restricted to its eastern part (cf. Pan et al., 2004; Zhu et al., 2012).

The Lhasa Terrane is widely considered an archetype of a Cenozoic orogen as a result of the India–Asia continental collision marked by the Indus–Yarlung Zangbo suture zone and a pre-Cretaceous Andean-type active continental margin genetically associated with the northward subduction of the Neo-Tethyan lithosphere (Allègre et al., 1984; Sengör, 1987; Yin and Harrison, 2000; Chung et al., 2005). Recent studies have indicated that the northward subduction of the Neo-Tethyan seafloor was likely initiated in the Cretaceous and triggered by the Lhasa–Qiangtang collision and that much of the Mesozoic magmatism in the Lhasa Terrane was associated with the southward subduction of the Bangong–Nujiang Tethyan lithosphere beneath the Lhasa Terrane. This south-directed subduction began in the late Middle Permian as a result of the Lhasa–Australia collision and ceased in the late Early Cretaceous (Zhu et al., 2009a, 2009b, 2010, 2011b, 2012). Tectonically, both the northern and southern Lhasa subterrane experienced significant crustal shortening (>50% and >40%, respectively) during the Late Cretaceous (cf. Kapp et al., 2003; He et al., 2007).

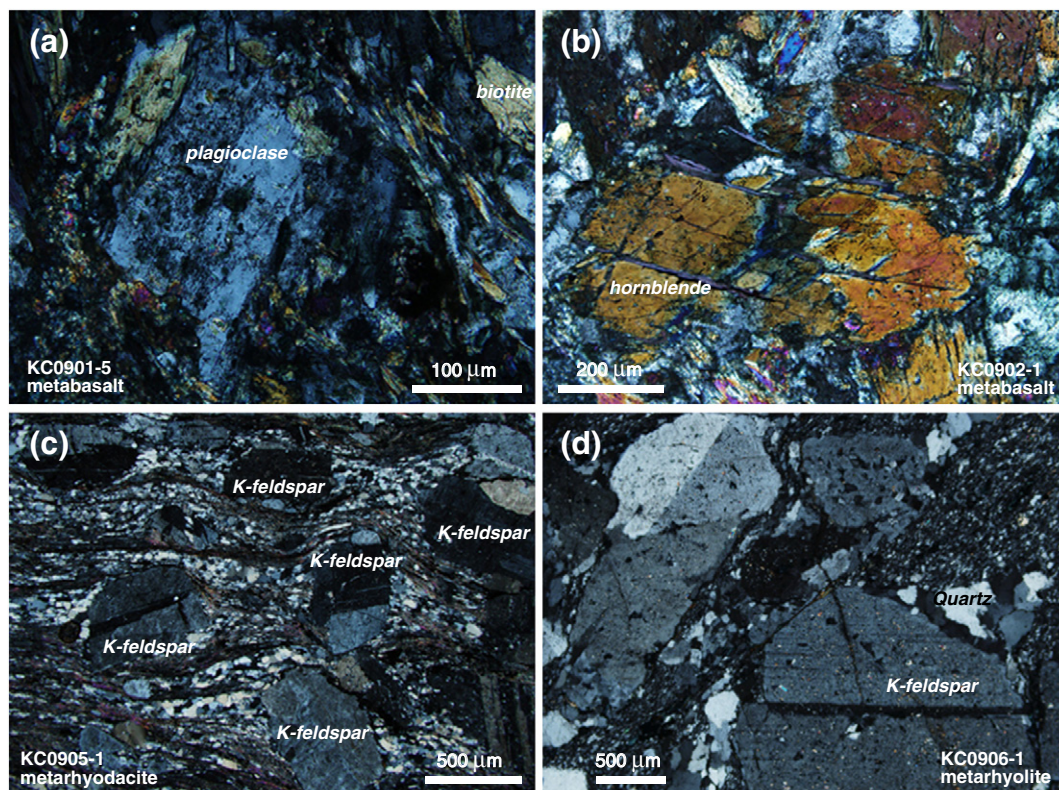


Fig. 2. Photomicrographs showing the porphyritic texture of the Cambrian metavolcanic rocks in the central Lhasa subterrane. Note that the groundmass minerals in all samples are altered and oriented due to post-magmatic events.

3. Field and petrographic observations

The Cambrian metavolcanic rocks are exposed to the east of Xainza and southeast of Nyima in the central Lhasa subterrane (Fig. 1b). Metavolcanic rocks in Xainza are intercalated with quartzite and slate with marble lenses (Ji et al., 2009a; Li et al., 2010), which have previously been assigned to the Nyainqêntanglha Group (Pan et al., 2004). They are composed of metarhyolite (~170 m thick in total) and metarhyolitic volcanoclastic rocks (Ji et al., 2009a) and are overlain unconformably by Ordovician clastic sequences with basal conglomerates that contain metarhyolitic material from the underlying strata (Li et al., 2010). Southeast of Nyima around Banglei village, the metavolcanic rocks are faulted against Silurian–Permian clastic rocks and are intruded by Cretaceous granitoids (Fig. 1c). The Banglei metavolcanic rocks are dominated by metarhyolite and metarhyolitic volcanoclastic rocks with subordinate metabasalts, forming a bimodal suite with a total thickness of ~1000 m. The metavolcanic rocks from both Xainza and Banglei experienced greenschist facies metamorphism, but some primary sedimentary structures (e.g., graded bedding and cross-bedding) are locally well preserved (Ji et al., 2009a).

The Banglei metabasalts (Fig. 1c; 31°25.158'N, 87°32.804'E, 5289 m) are extensively altered, but the original textures remain preserved. They are porphyric with plagioclase (5–10%) and hornblende phenocrysts (5–8%) (Fig. 2a and b) in a groundmass composed of oriented fine-grained plagioclase, altered minerals (e.g., chlorite, sericite), and magnetite (Fig. 2a). The Banglei silicic metavolcanic rocks are strongly foliated and show compositional banding composed of quartz and chlorite (Fig. 2c and d). Rotated porphyroclasts of K-feldspar (15–20%) and quartz (5–10%) are also present in these rocks (Fig. 2c and d).

4. Analytical methods

One metabasalt sample and five metarhyolite samples were selected for in situ zircon U–Pb and Hf isotope analysis. Zircons were separated for each sample by heavy-liquid and magnetic methods in the Laboratory of the Geological Team of Hebei Province, China. Cathodoluminescence (CL) images were taken at the Institute of Geology, Chinese Academy of Geological Sciences (Beijing) to inspect internal structures of individual zircons and to select positions for zircon isotope analyses. Zircon U–Pb dating with a beam size of 32 μm was conducted by LA-ICP-MS at the State Key Laboratory of Geological Processes and Mineral Resources, China University of Geosciences (Wuhan). The detailed operating conditions for the laser ablation system, the ICP-MS instrument and data reduction are the same as those described by Liu et al. (2008, 2010a). Off-line selection and the integration of background and analyses of signals, time-drift correction, U–Pb dating, and quantitative calibration for trace element analyses were performed by ICPMSDataCal (Liu et al., 2008, 2010a, 2010b). Trace element compositions of zircons were calibrated against multiple-reference materials (BCR-2G and BIR-1G) combined with internal standardization (Liu et al., 2010a). Common lead was corrected for by using the correction function (Andersen, 2002). ISOPLOT (version 3.0) (Ludwig, 2003) was used to plot concordia diagrams and for age calculations. Uncertainties of individual analyses are reported as 1 σ (Table S1); mean ages for pooled $^{206}\text{Pb}/^{238}\text{U}$ results are reported as 2 σ (Fig. 3). The obtained mean $^{206}\text{Pb}/^{238}\text{U}$ age for zircon standard GJ-1 with a beam size of 32 μm was 604.2 ± 2.0 Ma (2 σ , n = 24), consistent with the reported or recommended values (602.1 ± 4.9 Ma, Liu et al., 2010a; 599.8 ± 1.7 Ma, Jackson et al., 2004).

Major element compositions of whole-rock samples were determined by inductively coupled plasma-atomic emission spectroscopy (ICP-AES) at the China University of Geosciences (Beijing), with analytical uncertainties generally better than 5% (except P_2O_5) (Table S2). Trace element analyses were conducted by LA-ICP-MS at the State Key Laboratory of Geological Processes and Mineral Resources, China University of Geosciences (Wuhan). During analysis, data quality was monitored by analyses of USGS rock reference materials (BHVO-2, BCR-2,

AGV-2, and RGM-1). The detailed operating conditions for the laser ablation system, the ICP-MS instrument, and data reduction were the same as those described by Liu et al. (2008). The accuracy was generally better than 10%, with the exception of Sc, V, Cr, Ni, Y, and Dy in RGM-1 (rhyolite-USGS) and Cr in BCR-2 (basalt-USGS) rock standards, which differed by 10–15% from the reference values (Table S2). Whole-rock Sr–Nd isotopic compositions were determined using a Finnigan MAT-261 mass spectrometer operated in static mode at China University of Geosciences (Wuhan). Analytical details were given in Rudnick et al. (2004) and Liu et al. (2004). Sr and Nd isotopic fractionation was normalized to $^{86}\text{Sr}/^{88}\text{Sr} = 0.1194$ and $^{146}\text{Nd}/^{144}\text{Nd} = 0.7219$, respectively. The average $^{143}\text{Nd}/^{144}\text{Nd}$ ratio of the La Jolla standard measured during the sample runs was 0.511862 ± 5 (2 σ), and the average $^{87}\text{Sr}/^{86}\text{Sr}$ ratio of the NBS987 standard was 0.710236 ± 16 (2 σ). The total procedural Sr and Nd blanks were <1 ng and <50 pg, respectively. The whole-rock geochemical data are listed in Table 1.

In situ Hf isotope measurements were subsequently performed on the same spots or the same age domains for age determinations of the concordant grains, as guided by CL images. Zircons were performed using a Nu Plasma HR MC-ICP-MS (Nu Instruments Ltd., UK), coupled to a GeoLas 2005 excimer ArF laser ablation system with a beam size of 44 μm and a laser pulse frequency of 8 Hz at the State Key Laboratory of Continental Dynamics, Northwest University (Xi'an). Details on the instrumental conditions and data acquisition were given in Yuan et al. (2008). The measured values of well-characterized zircon standards (91500, GJ-1, and Monastery) agreed with the recommended values (cf. Yuan et al., 2008) to within 2 σ . The obtained Hf isotopic compositions were 0.282016 ± 20 (2 σ , n = 84) for the GJ-1 standard and 0.282735 ± 24 (2 σ , n = 84) for the Monastery standard, respectively, in agreement with the recommended values (cf. Yuan et al., 2008) to within 2 σ . The initial $^{176}\text{Hf}/^{177}\text{Hf}$ ratios and $\epsilon_{\text{Hf}}(t)$ values were calculated in reference to the chondritic reservoir (CHUR) at the time of zircon growth from magmas. Depleted mantle model ages (T_{DM}) used for metabasalt were calculated in reference to the depleted mantle at a present-day $^{176}\text{Hf}/^{177}\text{Hf}$ ratio of 0.28325 and $^{176}\text{Lu}/^{177}\text{Hf}$ of 0.0384 (Griffin et al., 2000). The Hf isotope crustal model ages (T_{DM}^{C}) used for zircons from metarhyolites were calculated by assuming its parental magma to have been derived from an average continental crust, with $^{176}\text{Lu}/^{177}\text{Hf} = 0.015$, that originated from the depleted mantle source (Griffin et al., 2002). Our conclusions would not be affected if other decay constants were used. The zircon Lu–Hf isotopic data are given in Table 2.

5. Results

5.1. Zircon U–Pb age and trace element data

The zircon grains from five metarhyolite samples were mostly euhedral to subhedral and showed short prismatic forms (50–150 μm long) with an aspect ratio of 1:1–2:1. They were transparent, colorless to pale brown, and exhibited clear oscillatory zoning (Fig. 3). A few zircon grains displayed dark, rounded or oval shapes and complex internal texture under CL. All of the analyzed zircons from five metarhyolite samples, excluding inherited cores, had varying uranium (105–4351 ppm) and thorium (62–7132 ppm) contents, with Th/U ratios ranging from 0.36 to 2.44 (Table S1), consistent with a magmatic origin (Hoskin and Schaltegger, 2003). Zircon grains from each metarhyolite sample yielded concordant or near-concordant $^{206}\text{Pb}/^{238}\text{U}$ ages, with a mean of ca. 492 Ma (Fig. 3). This age was interpreted as representing the timing of zircon crystallization and thus the timing of the formation of rhyolitic rocks. Seventeen analyses (including one rim) with Th/U > 0.1 from sample KC0906-1 yielded an age cluster at ca. 538 Ma. A similar age was also documented by zircon grains from sample KC0902-3 (Fig. 3). We interpreted this older age as the timing of early magmatic activity in the region.

Most zircon grains from the metabasalt sample (KC0901-2) were rounded or oval, with inherited cores and overgrown rims, but one

Table 1
Whole-rock major, trace element and Sr–Nd isotopic data of the Cambrian metavolcanic rocks in the central Lhasa subterrane, southern Tibet.

Sample no.	KC0901-1	KC0901-2	KC0901-4	KC0901-5	KC0901-6	KC0902-1	KC0902-2	KC0902-3	KC0903-1	KC0903-2	KC0904-1	KC0904-2	KC0905-1	KC0906-1	KC0906-1R
<i>ICP-AES – major element (wt.%)</i>															
SiO ₂	75.88	48.05	75.76	51.40	75.67	48.96	72.54	76.29	51.12	74.22	48.06	78.62	66.23	74.10	
TiO ₂	0.34	2.42	0.38	1.37	0.45	1.32	0.56	0.32	1.58	0.46	1.92	0.31	0.69	0.43	
Al ₂ O ₃	12.13	13.53	12.26	13.77	10.69	13.38	12.87	12.03	14.52	12.75	13.96	10.49	16.07	12.38	
Fe ₂ O ₃	2.06	17.54	2.23	12.70	4.03	13.21	4.12	2.41	12.91	2.12	16.25	1.90	5.52	2.36	
MnO	0.03	0.23	0.04	0.25	0.07	0.30	0.08	0.03	0.27	0.04	0.26	0.02	0.06	0.03	
MgO	0.35	4.57	0.42	6.26	0.87	7.97	0.89	0.37	5.24	0.38	5.80	0.32	1.60	0.53	
CaO	0.45	5.14	0.62	6.98	0.60	9.15	0.73	0.71	6.66	1.02	5.97	0.70	0.69	0.42	
Na ₂ O	5.49	0.81	4.37	3.55	3.99	2.04	4.86	4.45	3.85	5.47	2.43	3.73	2.92	3.24	
K ₂ O	1.99	5.56	3.67	1.22	1.97	1.81	2.39	3.05	1.23	2.31	4.35	2.77	4.01	4.85	
P ₂ O ₅	0.10	0.44	0.06	0.15	0.08	0.03	0.07	0.09	0.27	0.09	0.26	0.02	0.09	0.11	
LOI	0.56	1.48	0.42	1.71	0.76	1.93	0.74	0.58	1.84	0.36	1.14	0.69	1.93	0.81	
Total	99.37	99.77	100.22	99.35	99.18	100.09	99.86	100.32	99.47	99.21	100.39	99.58	99.82	99.26	
Mg#	25	34	27	50	30	55	30	24	45	26	42	25	37	31	
<i>ICP-MS – trace element (ppm)</i>															
Sc	7.21	45.6	7.84	43.0	10.6	56.0	11.9	6.59	39.6	7.51	22.4	6.16	13.3	8.31	7.91
V	13.5	397	16.0	320	37.6	322	33.4	11.7	318	22.5	234	16.7	57.5	21.4	20.4
Cr	2.50	54.5	3.03	198	21.1	296	19.2	2.04	148	3.07	29.2	2.40	10.6	5.96	5.68
Co	2.62	46.2	2.56	43.7	5.76	49.5	5.08	2.31	39.4	2.74	24.3	2.03	5.32	2.06	1.96
Ni	1.68	35.5	1.62	78.4	10.3	83.8	8.30	1.59	62.2	2.18	22.6	1.46	5.48	3.06	2.92
Ga	13.7	24.6	12.8	22.2	14.1	19.8	15.3	13.8	25.5	12.6	13.0	10.9	21.7	14.0	13.4
Rb	66.5	593	129	94.6	101	112	108	99.6	76.7	70.0	193	86.3	319	214	200
Sr	32.7	93.4	31.6	169	50.9	166	62.0	65.1	173	37.0	55.5	40.1	45.0	42.9	44.1
Y	39.7	61.1	39.0	38.4	21.7	27.9	26.6	28.6	57.1	34.2	25.0	30.0	53.7	24.4	23.3
Zr	245	163	270	141	175	54.1	221	245	184	292	71.0	200	362	264	251
Nb	14.6	10.1	14.7	6.82	10.6	2.09	13.0	13.6	8.61	15.9	3.63	11.9	21.2	15.9	15.0
Cs	1.31	110	2.74	6.68	6.49	3.69	7.39	2.11	3.34	2.62	36.6	2.35	10.6	5.51	5.34
Ba	267	690	585	218	449	254	624	583	237	422	235	444	976	811	788
La	46.6	27.9	42.5	15.2	24.3	5.10	29.5	29.6	23.4	39.9	10.9	35.5	57.3	23.7	22.7
Ce	85.3	53.8	80.4	31.6	50.7	10.3	60.3	71.4	50.3	77.3	22.9	65.5	108	57.5	55.3

Pr	9.72	7.23	8.72	4.24	5.67	1.70	6.77	6.77	6.25	8.38	2.95	7.50	11.9	5.43	5.29
Nd	35.0	31.1	31.8	18.3	20.8	8.74	24.8	24.4	26.6	30.6	12.8	27.0	43.1	19.8	18.8
Sm	6.75	7.79	6.26	4.87	4.16	2.86	4.97	4.74	6.55	5.96	3.11	5.16	8.39	3.81	3.59
Eu	0.82	2.08	0.82	1.34	0.99	1.04	1.17	0.67	2.26	0.79	0.87	0.75	1.24	0.59	0.58
Gd	6.16	8.51	5.75	5.57	3.85	3.84	4.62	4.51	7.70	5.31	3.51	4.83	7.98	3.54	3.44
Tb	1.01	1.48	0.98	1.00	0.63	0.71	0.77	0.76	1.36	0.90	0.61	0.83	1.34	0.62	0.60
Dy	6.29	9.54	6.24	6.66	3.87	4.82	4.72	4.86	8.90	5.65	3.90	5.12	8.43	4.12	3.99
Ho	1.25	1.97	1.26	1.39	0.78	1.02	0.94	1.00	1.84	1.17	0.82	1.05	1.71	0.89	0.86
Er	3.64	5.63	3.76	3.98	2.28	2.99	2.83	3.09	5.34	3.60	2.35	3.05	5.20	2.85	2.73
Tm	0.57	0.83	0.58	0.60	0.33	0.44	0.43	0.50	0.79	0.57	0.36	0.46	0.79	0.48	0.46
Yb	3.65	5.49	3.91	4.01	2.29	2.87	2.87	3.41	5.18	3.85	2.31	3.11	5.17	3.26	3.15
Lu	0.56	0.81	0.58	0.62	0.35	0.43	0.44	0.52	0.79	0.59	0.35	0.48	0.79	0.54	0.55
Hf	6.59	4.32	7.16	3.66	4.40	1.68	5.76	6.65	4.93	7.89	1.88	5.51	9.63	7.11	6.99
Ta	1.38	0.75	1.39	0.51	0.85	0.15	1.11	1.32	0.68	1.50	0.27	1.13	1.85	1.44	1.38
Pb	29.0	20.6	26.8	16.2	34.0	34.9	32.7	27.4	23.5	46.0	27.2	27.4	24.8	15.9	15.3
Th	24.7	6.56	24.5	5.04	11.2	0.72	15.0	22.3	7.55	23.1	3.08	19.0	30.0	21.7	21.1
U	3.05	1.21	3.56	0.97	1.61	0.16	2.05	3.42	1.53	3.93	0.56	2.65	3.41	3.08	2.98

Sr–Nd isotope compositions

$^{87}\text{Rb}/^{86}\text{Sr}$	5.90	18.36	11.79	1.63	5.74	1.95	5.04	4.43	1.28	5.48	10.09	6.23	20.56	14.47
$^{87}\text{Sr}/^{86}\text{Sr}$	0.767474	0.771877	0.793058	0.738471	0.759913	0.731348	0.759107	0.751962	0.736381	0.755872	0.760993	0.765865	0.816313	0.796966
$\pm 2\sigma$	0.000003	0.000003	0.000004	0.000004	0.000004	0.000004	0.000005	0.000003	0.000005	0.000004	0.000004	0.000004	0.000005	0.000004
$^{147}\text{Sm}/^{144}\text{Nd}$	0.1166	0.1516	0.1192	0.1607	0.1209	0.1976	0.1213	0.1177	0.1488	0.1178	0.1472	0.1157	0.1176	0.1162
$^{143}\text{Nd}/^{144}\text{Nd}$	0.512008	0.512252	0.512001	0.512328	0.511966	0.512657	0.511990	0.511997	0.512304	0.511992	0.512289	0.512004	0.512000	0.512008
$\pm 2\sigma$	0.000003	0.000004	0.000003	0.000002	0.000003	0.000003	0.000004	0.000002	0.000004	0.000004	0.000005	0.000004	0.000002	0.000005
$(^{87}\text{Sr}/^{86}\text{Sr})_i$	0.7261	0.6432	0.7104	0.7271	0.7197	0.7177	0.7238	0.7209	0.7274	0.7175	0.6902	0.7222	0.6722	0.6955
$(^{143}\text{Nd}/^{144}\text{Nd})_i$	0.51163	0.51176	0.51162	0.51181	0.51158	0.51202	0.51160	0.51162	0.51182	0.51161	0.51181	0.51163	0.51162	0.51163
$\epsilon_{\text{Nd}}(t)$	−7.3	−4.7	−7.6	−3.8	−8.4	0.3	−7.9	−7.5	−3.5	−7.7	−3.7	−7.3	−7.5	−7.2
T_{DM} (Ma)	1792		1851		1943		1911	1830		1839		1782	1822	1785
T_{DM2} (Ma)	1810		1834		1899		1862	1833		1842		1812	1828	1808

LOI = loss on ignition. Mg# = $100 \times \text{Mg}^{2+} / (\text{Mg}^{2+} + \text{TFe}^{2+})$, TFeO* = $0.9 \times \text{TFe}_2\text{O}_3$. Corrected formulas are as follows: $(^{87}\text{Sr}/^{86}\text{Sr})_i = (^{87}\text{Sr}/^{86}\text{Sr})_{\text{sample}} - ^{87}\text{Rb}/^{86}\text{Sr} (e^{\lambda t} - 1)$, $\lambda = 1.42 \times 10^{-11} \text{ a}^{-1}$; $(^{143}\text{Nd}/^{144}\text{Nd})_i = (^{143}\text{Nd}/^{144}\text{Nd})_{\text{sample}} - (^{147}\text{Sm}/^{144}\text{Nd})_{\text{m}} \times (e^{\lambda t} - 1)$, $\epsilon_{\text{Nd}}(t) = [(^{143}\text{Nd}/^{144}\text{Nd})_{\text{sample}} / (^{143}\text{Nd}/^{144}\text{Nd})_{\text{CHUR}}(t) - 1] \times 10^4$, $(^{143}\text{Nd}/^{144}\text{Nd})_{\text{CHUR}}(t) = 0.512638 - 0.1967 \times (e^{\lambda t} - 1)$, $T_{\text{DM}} = 1/\lambda \times \ln \{1 + [((^{143}\text{Nd}/^{144}\text{Nd})_{\text{sample}} - 0.51315) / ((^{147}\text{Sm}/^{144}\text{Nd})_{\text{sample}} - 0.21317)]\}$, $\lambda_{\text{Sm-Nd}} = 6.54 \times 10^{-12} \text{ a}^{-1}$; T_{DM2} is the two-stage Nd depleted-mantle model age calculated using the same assumption formulation as [Keto and Jacobsen \(1987\)](#).

Table 2
Hf isotopic data of zircon grains from the Cambrian metavolcanic rocks in the central Lhasa subterrane, southern Tibet.

No.	Age (Ma)	$^{176}\text{Yb}/$ ^{177}Hf	$^{176}\text{Lu}/$ ^{177}Hf	$^{176}\text{Hf}/$ ^{177}Hf	2σ	$^{176}\text{Hf}/$ $^{177}\text{Hf}_t$	$\epsilon_{\text{Hf}}(0)$	$\epsilon_{\text{Hf}}(t)$	T_{DM} (Ma)	T_{DM}^c (Ma)	$f_{\text{Lu/Hf}}$
<i>Sample KC0901-1, metarhyolite</i>											
KC0901-1-02	489	0.027820	0.000930	0.282231	0.000036	0.282222	-19.1	-9.0	1438	1997	-0.97
KC0901-1-03	492	0.025052	0.000936	0.282067	0.000086	0.282059	-24.9	-14.7	1665	2355	-0.97
KC0901-1-04	489	0.023589	0.000814	0.282234	0.000038	0.282227	-19.0	-8.8	1428	1986	-0.98
KC0901-1-06	492	0.078287	0.002519	0.282183	0.000058	0.282160	-20.8	-11.1	1569	2131	-0.92
KC0901-1-08	491	0.030092	0.000989	0.282212	0.000046	0.282203	-19.8	-9.6	1466	2037	-0.97
KC0901-1-09	492	0.032042	0.001069	0.282200	0.000040	0.282190	-20.2	-10.1	1486	2066	-0.97
KC0901-1-10	491	0.033969	0.001104	0.282224	0.000044	0.282214	-19.4	-9.3	1453	2013	-0.97
KC0901-1-11	494	0.030049	0.000996	0.282209	0.000046	0.282200	-19.9	-9.7	1471	2043	-0.97
KC0901-1-13	531	0.120291	0.003623	0.282108	0.000035	0.282071	-23.5	-13.4	1731	2301	-0.89
KC0901-1-15	492	0.033508	0.001131	0.282239	0.000041	0.282229	-18.9	-8.7	1434	1981	-0.97
KC0901-1-16	551	0.151016	0.004570	0.282109	0.000049	0.282062	-23.4	-13.3	1776	2309	-0.86
KC0901-1-17	489	0.090453	0.002792	0.282179	0.000050	0.282153	-21.0	-11.5	1588	2149	-0.92
KC0901-1-18	494	0.020341	0.000676	0.282254	0.000044	0.282247	-18.3	-8.0	1396	1938	-0.98
KC0901-1-19	491	0.030611	0.001144	0.282272	0.000064	0.282262	-17.7	-7.6	1387	1907	-0.97
KC0901-1-20	491	0.042288	0.001326	0.282256	0.000038	0.282244	-18.2	-8.2	1417	1947	-0.96
KC0901-1-23	501	0.031397	0.000987	0.282243	0.000044	0.282234	-18.7	-8.3	1423	1964	-0.97
KC0901-1-24	491	0.026448	0.000826	0.282267	0.000032	0.282260	-17.8	-7.6	1383	1912	-0.98
KC0901-1-25	546	0.034899	0.001133	0.282181	0.000042	0.282170	-20.9	-9.6	1514	2077	-0.97
KC0901-1-28	492	0.050735	0.001609	0.282202	0.000053	0.282187	-20.2	-10.2	1504	2071	-0.95
KC0901-1-29	492	0.034856	0.001232	0.282168	0.000068	0.282157	-21.4	-11.3	1537	2139	-0.96
KC0901-1-31	490	0.029836	0.000967	0.282258	0.000045	0.282249	-18.2	-8.0	1401	1937	-0.97
KC0901-1-32	493	0.107121	0.003377	0.282224	0.000051	0.282193	-19.4	-10.0	1546	2058	-0.90
KC0901-1-34	489	0.036799	0.001194	0.282190	0.000043	0.282179	-20.6	-10.5	1504	2091	-0.96
KC0901-1-35	492	0.070721	0.002154	0.282129	0.000060	0.282109	-22.7	-13.0	1632	2244	-0.94
KC0901-1-36	541	0.029734	0.000920	0.282226	0.000044	0.282217	-19.3	-8.1	1444	1976	-0.97
KC0901-1-39	491	0.048962	0.001608	0.282209	0.000054	0.282194	-19.9	-10.0	1495	2058	-0.95
KC0901-1-42	490	0.045531	0.001546	0.282220	0.000107	0.282205	-19.5	-9.6	1477	2033	-0.95
<i>Sample KC0901-2, metabasalt</i>											
KC0901-2-01	491	0.028228	0.000968	0.282555	0.000180	0.282546	-7.7	2.5	986	1276	-0.97
KC0901-2-02	492	0.050043	0.001623	0.282701	0.000060	0.282686	-2.5	7.5	793	962	-0.95
KC0901-2-03	491	0.038202	0.001262	0.282468	0.000060	0.282456	-10.7	-0.7	1116	1475	-0.96
KC0901-2-04	1261	0.023696	0.000861	0.282157	0.000073	0.282136	-21.8	5.4	1537	1701	-0.97
KC0901-2-05	493	0.051481	0.001738	0.282652	0.000079	0.282636	-4.2	5.7	866	1074	-0.95
KC0901-2-06	1759	0.032263	0.001182	0.281896	0.000198	0.281857	-31.0	6.9	1914	2003	-0.96
<i>Sample KC0902-3, metarhyolite</i>											
KC0902-3-01	1021	0.005937	0.000211	0.282209	0.000030	0.282204	-19.9	2.3	1441	1701	-0.99
KC0902-3-04	491	0.200144	0.006480	0.282318	0.000050	0.282258	-16.1	-7.7	1542	1914	-0.80
KC0902-3-07	492	0.049209	0.001717	0.282290	0.000079	0.282275	-17.0	-7.1	1383	1878	-0.95
KC0902-3-08	492	0.024334	0.000860	0.282332	0.000053	0.282324	-15.5	-5.3	1294	1768	-0.97
KC0902-3-09	534	0.035717	0.001177	0.282331	0.000068	0.282319	-15.6	-4.6	1306	1753	-0.96
KC0902-3-10	492	0.054097	0.001894	0.282283	0.000045	0.282266	-17.3	-7.4	1400	1898	-0.94
KC0902-3-11	493	0.031454	0.001140	0.282246	0.000061	0.282236	-18.6	-8.4	1424	1964	-0.97
KC0902-3-12	530	0.144791	0.004775	0.282164	0.000041	0.282116	-21.5	-11.9	1703	2203	-0.86
KC0902-3-13	492	0.029038	0.001036	0.282335	0.000050	0.282325	-15.5	-5.3	1297	1767	-0.97
KC0902-3-14	538	0.125685	0.004074	0.282093	0.000039	0.282052	-24.0	-13.9	1776	2340	-0.88
KC0902-3-15	494	0.037306	0.001299	0.282234	0.000045	0.282222	-19.0	-8.9	1447	1994	-0.96
KC0902-3-16	493	0.077371	0.002581	0.282303	0.000038	0.282279	-16.6	-6.9	1398	1868	-0.92
KC0902-3-17	492	0.029357	0.001015	0.282292	0.000045	0.282282	-17.0	-6.8	1356	1861	-0.97
KC0902-3-18	492	0.024213	0.000866	0.282331	0.000036	0.282323	-15.6	-5.4	1295	1771	-0.97
<i>Sample KC0905-1, metarhyolite</i>											
KC0905-1-01	741	0.054372	0.001869	0.282367	0.000038	0.282341	-14.3	0.8	1280	1576	-0.94
KC0905-1-02	510	0.073796	0.002468	0.282260	0.000040	0.282236	-18.1	-8.0	1456	1952	-0.93
KC0905-1-03	492	0.060975	0.002139	0.282338	0.000035	0.282318	-15.4	-5.6	1331	1782	-0.94
KC0905-1-04	493	0.042688	0.001558	0.282268	0.000053	0.282254	-17.8	-7.8	1409	1924	-0.95
KC0905-1-05	492	0.032911	0.001151	0.282310	0.000038	0.282299	-16.4	-6.2	1335	1824	-0.97
KC0905-1-06	492	0.060398	0.002099	0.282319	0.000059	0.282300	-16.0	-6.2	1356	1822	-0.94
KC0905-1-08	493	0.031924	0.001115	0.282282	0.000039	0.282272	-17.3	-7.2	1373	1884	-0.97
KC0905-1-09	492	0.018496	0.000681	0.282215	0.000054	0.282209	-19.7	-9.4	1449	2023	-0.98
KC0905-1-10	494	0.018947	0.000705	0.282344	0.000040	0.282338	-15.1	-4.8	1272	1738	-0.98
KC0905-1-12	493	0.028415	0.000973	0.282255	0.000035	0.282246	-18.3	-8.1	1405	1940	-0.97
KC0905-1-13	492	0.033632	0.001209	0.282284	0.000055	0.282273	-17.3	-7.2	1373	1882	-0.96
KC0905-1-14	492	0.021071	0.000752	0.282318	0.000037	0.282311	-16.1	-5.8	1310	1798	-0.98
KC0905-1-15	510	0.044309	0.001480	0.282310	0.000045	0.282296	-16.3	-5.9	1347	1821	-0.96
KC0905-1-16	493	0.033347	0.001190	0.282288	0.000048	0.282277	-17.1	-7.0	1368	1874	-0.96
KC0905-1-17	701	0.045179	0.001575	0.282075	0.000038	0.282054	-24.6	-10.2	1682	2234	-0.95
KC0905-1-18	491	0.025293	0.000872	0.282278	0.000045	0.282270	-17.5	-7.3	1370	1890	-0.97

Table 2 (continued)

No.	Age (Ma)	$^{176}\text{Yb}/$ ^{177}Hf	$^{176}\text{Lu}/$ ^{177}Hf	$^{176}\text{Hf}/$ ^{177}Hf	2σ	$^{176}\text{Hf}/$ $^{177}\text{Hf}_f$	$\epsilon_{\text{Hf}}(0)$	$\epsilon_{\text{Hf}}(t)$	T_{DM} (Ma)	T_{DM}^c (Ma)	$f_{\text{Lu/Hf}}$
<i>Sample KC0906-1, metarhyolite</i>											
KC0906-1-01	495	0.058729	0.002003	0.282324	0.000043	0.282305	-15.8	-5.9	1346	1808	-0.94
KC0906-1-02	528	0.034815	0.001277	0.282277	0.000044	0.282264	-17.5	-6.7	1386	1879	-0.96
KC0906-1-03	495	0.048533	0.001703	0.282241	0.000064	0.282225	-18.8	-8.8	1453	1986	-0.95
KC0906-1-04	488	0.063824	0.002140	0.282326	0.000040	0.282307	-15.8	-6.0	1347	1809	-0.94
KC0906-1-05	490	0.081503	0.002935	0.282294	0.000053	0.282267	-16.9	-7.4	1425	1896	-0.91
KC0906-1-06	491	0.024986	0.000846	0.282243	0.000030	0.282236	-18.7	-8.5	1417	1966	-0.97
KC0906-1-07	494	0.020406	0.000708	0.282210	0.000039	0.282204	-19.9	-9.6	1458	2034	-0.98
KC0906-1-09	496	0.016603	0.000589	0.282198	0.000034	0.282192	-20.3	-9.9	1470	2058	-0.98
KC0906-1-10	541	0.042058	0.001401	0.282257	0.000040	0.282243	-18.2	-7.1	1418	1917	-0.96
KC0906-1-12	489	0.046421	0.001598	0.282281	0.000046	0.282267	-17.4	-7.4	1392	1898	-0.95
KC0906-1-13	540	0.017566	0.000609	0.282278	0.000039	0.282272	-17.5	-6.1	1360	1855	-0.98
KC0906-1-14	489	0.030757	0.001047	0.282256	0.000047	0.282246	-18.3	-8.2	1407	1943	-0.97
KC0906-1-16	492	0.041402	0.001335	0.282316	0.000040	0.282304	-16.1	-6.1	1333	1813	-0.96
KC0906-1-19	535	0.032160	0.001073	0.282175	0.000045	0.282164	-21.1	-10.0	1521	2096	-0.97
KC0906-1-20	534	0.036453	0.001290	0.282194	0.000048	0.282182	-20.4	-9.4	1502	2058	-0.96
KC0906-1-21	532	0.043566	0.001450	0.282308	0.000037	0.282294	-16.4	-5.5	1348	1811	-0.96
KC0906-1-22	530	0.017758	0.000599	0.282300	0.000032	0.282294	-16.7	-5.5	1329	1811	-0.98
KC0906-1-24	493	0.024238	0.000820	0.282198	0.000040	0.282190	-20.3	-10.1	1479	2065	-0.98
KC0906-1-25	530	0.024034	0.000828	0.282294	0.000038	0.282286	-16.9	-5.8	1346	1830	-0.98
KC0906-1-26	492	0.093684	0.003065	0.282326	0.000042	0.282298	-15.8	-6.3	1382	1826	-0.91
KC0906-1-27	489	0.022168	0.000794	0.282292	0.000044	0.282285	-17.0	-6.8	1348	1859	-0.98
KC0906-1-28	492	0.022093	0.000775	0.282263	0.000039	0.282256	-18.0	-7.7	1386	1919	-0.98
KC0906-1-29	496	0.017762	0.000642	0.282262	0.000036	0.282256	-18.0	-7.7	1383	1917	-0.98
KC0906-1-31	493	0.022962	0.000755	0.282210	0.000049	0.282203	-19.9	-9.6	1460	2037	-0.98
KC0906-1-32	491	0.026426	0.000926	0.282215	0.000036	0.282206	-19.7	-9.5	1460	2030	-0.97
KC0906-1-33	539	0.029213	0.001030	0.282249	0.000038	0.282239	-18.5	-7.3	1415	1928	-0.97
KC0906-1-40	536	0.027616	0.001066	0.282280	0.000036	0.282270	-17.4	-6.3	1373	1862	-0.97
KC0906-1-60	531	0.037364	0.001372	0.282274	0.000046	0.282260	-17.6	-6.7	1394	1886	-0.96

$$\epsilon_{\text{Hf}}(t) = 10,000 \times \left\{ \left[\frac{(^{176}\text{Hf}/^{177}\text{Hf})_S - (^{176}\text{Lu}/^{177}\text{Hf})_S \times (e^{\lambda t} - 1)}{(^{176}\text{Hf}/^{177}\text{Hf})_{\text{CHUR},0} - (^{176}\text{Lu}/^{177}\text{Hf})_{\text{CHUR}} \times (e^{\lambda t} - 1)} \right] - 1 \right\}$$

$$T_{\text{DM}} = 1/\lambda \times \ln \left\{ 1 + \left[\frac{(^{176}\text{Hf}/^{177}\text{Hf})_S - (^{176}\text{Lu}/^{177}\text{Hf})_{\text{DM}}}{(^{176}\text{Lu}/^{177}\text{Hf})_S - (^{176}\text{Lu}/^{177}\text{Hf})_{\text{DM}}} \right] - 1 \right\}$$

$$T_{\text{DM}}^c = T_{\text{DM}} - (T_{\text{DM}} - t) \times \left[\frac{(f_{\text{cc}} - f_s)}{(f_{\text{cc}} - f_{\text{DM}})} \right]$$

$$f_{\text{Lu/Hf}} = \frac{(^{176}\text{Lu}/^{177}\text{Hf})_S}{(^{176}\text{Lu}/^{177}\text{Hf})_{\text{CHUR}} - 1}$$

where, $\lambda = 1.867 \times 10^{-11} \text{ year}^{-1}$ (Soderlund et al., 2004); $(^{176}\text{Lu}/^{177}\text{Hf})_S$ and $(^{176}\text{Hf}/^{177}\text{Hf})_S$ are the measured values of the samples; $(^{176}\text{Lu}/^{177}\text{Hf})_{\text{CHUR}} = 0.0336$ and $(^{176}\text{Hf}/^{177}\text{Hf})_{\text{CHUR},0} = 0.282785$ (Bouvier et al., 2008); $(^{176}\text{Lu}/^{177}\text{Hf})_{\text{DM}} = 0.0384$ and $(^{176}\text{Hf}/^{177}\text{Hf})_{\text{DM}} = 0.28325$ (Griffin et al., 2000); $(^{176}\text{Lu}/^{177}\text{Hf})_{\text{mean crust}} = 0.015$; $f_{\text{cc}} = [(^{176}\text{Lu}/^{177}\text{Hf})_{\text{mean crust}} / (^{176}\text{Lu}/^{177}\text{Hf})_{\text{CHUR}} - 1]$; $f_s = f_{\text{Lu/Hf}}$; $f_{\text{DM}} = [(^{176}\text{Lu}/^{177}\text{Hf})_{\text{DM}} / (^{176}\text{Lu}/^{177}\text{Hf})_{\text{CHUR}} - 1]$; t = crystallization time of zircon.

zircon grain displayed a long-prismatic crystal form with rhythmic zoning (Fig. 3), which is a typical internal feature of zircons crystallized from mafic magmas. This zircon yielded a near-concordant $^{206}\text{Pb}/^{238}\text{U}$ age of 492 ± 4 Ma, identical to the $^{206}\text{Pb}/^{238}\text{U}$ ages of 493–491 Ma obtained from the other three zircon grains from this sample (Fig. 3; Table S1). Thus, we interpreted the age of ca. 492 Ma to represent the timing of basaltic eruption, which is coeval with the formation of the rhyolitic rocks.

Zircon grains from metarhyolites displayed fractionated rare-earth element (REE) patterns of heavy REE (HREE) enrichment and light REE (LREE) depletion, with clear negative Eu and positive Ce anomalies (Fig. 4a), as observed in magmatic zircons (Hoskin and Schaltegger, 2003). The ca. 492 Ma and ca. 538 Ma zircon grains had relatively low $(\text{Nb}/\text{Pb})_{\text{N}}$ ratios (hereafter, N denotes normalized to the chondrite values of Sun and McDonough (1989)) and Eu/Eu^* values that were comparable with those of S-type granites but lower than those of I-type granites (Fig. 4b; Wang et al., 2012).

5.2. Whole-rock major and trace element data

Field and petrographical observations indicated that the Cambrian metavolcanic rocks in the central Lhasa subterrane were metamorphosed under greenschist facies conditions and were variably altered (Fig. 2), resulting in modification of the concentrations of fluid-mobile elements (e.g., Na, K, Ca, Cs, Rb, Ba, and Sr). Therefore, in this study, we used only the immobile elements [e.g., high field strength elements (HFSEs) and REEs], transitional elements, and Nd isotopic compositions for rock classification and further discussion of tectonic setting and petrogenesis of the analyzed rocks.

The Cambrian metavolcanic samples showed a bimodal distribution in SiO_2 values between 48.42–52.64 wt.% and 67.66–79.51 wt.%

(normalized to an anhydrous basis), with a compositional gap of ca. 15 wt.%, and plot in the basalt and rhyodacite–rhyolite fields on the SiO_2 –Zr/TiO₂ classification diagram (Winchester and Floyd, 1977) (Fig. 5a). Metabasaltic rocks had varying MgO (4.65–8.12 wt.%) and Mg# (34–55), low Al₂O₃ (13.63–14.87 wt.%) (Fig. 5b), and low Cr (29–296 ppm) and Ni (22.6–83.8 ppm) values (Fig. 5c; Table 1). On the Th–Co plot (Hastie et al., 2007), which is especially effective for altered volcanic rocks, the metabasaltic and silicic metavolcanic rocks mostly plot in the high-K calc-alkaline and shoshonite fields (Fig. 5d).

The metabasaltic rocks, except for sample KC0902-1, showed similar chondrite-normalized REE patterns, with varying LREE enrichment ($[\text{La}/\text{Yb}]_{\text{N}} = 2.7$ –3.7) and discernible negative Eu anomalies ($\text{Eu}/\text{Eu}^* = 0.78$ –0.97) (Fig. 6a). Sample KC0902-1 displayed a flat REE pattern with similar abundances of HREE to those of N-MORB (Sun and McDonough, 1989). In the primitive mantle-normalized variation diagrams, the metabasalt samples showed enrichment in Th and LREE and depletion in Nb, Ta, P, and Ti (Fig. 6b), with low $(\text{Nb}/\text{La})_{\text{PM}}$ ratios (0.32–0.43) that resemble Andean arc basalts ($[\text{Nb}/\text{La}]_{\text{PM}} = 0.17$ –0.35; Hickey et al., 1986). The silicic metavolcanic rocks were generally enriched in LREEs ($[\text{La}/\text{Yb}]_{\text{N}} = 5.18$ –9.16), with moderate negative Eu anomalies ($\text{Eu}/\text{Eu}^* = 0.39$ –0.75) (Fig. 6c). Their primitive mantle-normalized variation diagrams show remarkable enrichments in Th and U and depletions in Nb, P and Ti relative to neighboring elements (Fig. 6d).

5.3. Whole-rock Sr and Nd isotopic data

The Cambrian metavolcanic rocks exhibited abnormally low initial Sr isotopic ratios (as low as 0.6432 for metabasalts and 0.6722 for silicic metavolcanic rocks; Table 1). Such unusual isotopic ratios have no petrogenetic significance because of the mobility of Rb and the timing of its addition to the rock systems, which led to the excessive

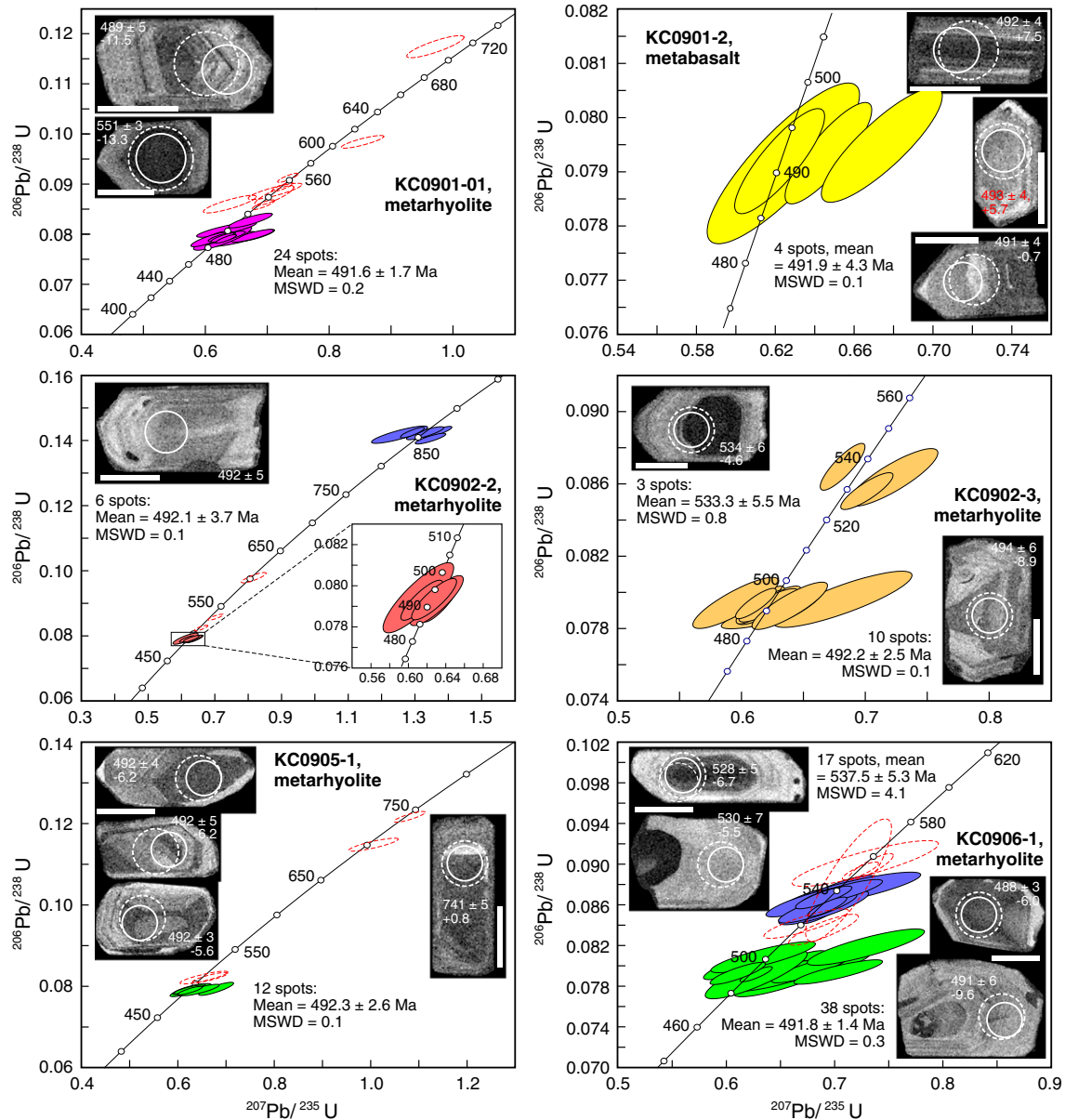


Fig. 3. Cathodoluminescence (CL) images of representative zircon grains and concordia plots of the metavolcanic rocks in the central Lhasa subterrane. Solid and dashed circles indicate the locations of LA-ICP-MS U–Pb dating and Hf analyses, respectively. The scale bar length in CL image is 50 μm .

subtraction of $^{87}\text{Rb}/^{86}\text{Sr}$ ratios (Table 1). One metabasalt sample (KC0902-1) exhibited a significantly higher $\varepsilon_{\text{Nd}}(t)$ value (+0.3) than the other four metabasalt samples, which displayed moderate negative $\varepsilon_{\text{Nd}}(t)$ values of -4.7 to -3.5 (corrected to 492 Ma). By contrast, the silicic metavolcanic samples had a restricted range of $\varepsilon_{\text{Nd}}(t)$ values ranging from -8.4 to -7.2 (Table 1), close to the $\varepsilon_{\text{Nd}}(t)$ values of the coeval granitoids from the Baoshan Terrane (ca. 500–493 Ma; $\varepsilon_{\text{Nd}}(t) = -9.7$ to -9.4 ; Liu et al., 2009) and northern Burma (ca. 491 Ma; $\varepsilon_{\text{Nd}}(t) = -10.8$; Mitchell et al., in press).

5.4. Zircon Lu–Hf isotopic data

Four zircon grains with $^{206}\text{Pb}/^{238}\text{U}$ ages of ca. 492 Ma from the metabasaltic rock sample (KC0901-2) yielded a relatively wide range of $\varepsilon_{\text{Hf}}(t)$ from -0.7 to $+7.5$ (Table 2). The youngest cluster with $^{206}\text{Pb}/^{238}\text{U}$ ages of ca. 492 Ma from four silicic metavolcanic samples (62 analyses) showed exclusively negative zircon $\varepsilon_{\text{Hf}}(t)$ values from -14.7 to -4.8 (inset in Fig. 7b), yielding Paleoproterozoic Hf crustal model ages (T_{DM}^{C}) of 1.7–2.4 Ga (Fig. 7b; Table 2), similar to the two-

stage Nd model ages (T_{DM2}) of 1.8–1.9 Ga (Table 1). The older cluster with $^{206}\text{Pb}/^{238}\text{U}$ ages of ca. 538 Ma (13 analyses) from three silicic metavolcanic samples (KC0901-1, KC0902-3, and KC0906-1) displayed zircon $\varepsilon_{\text{Hf}}(t)$ values of -13.9 to -4.6 , which were identical to those of the youngest cluster of ca. 492 Ma (Fig. 7b; Table 2). The zircon Hf isotopic compositions of the silicic metavolcanic rocks from the central Lhasa subterrane were comparable to those of the coeval granitoids from the Amdo [ca. 492 Ma; $\varepsilon_{\text{Hf}}(t) = -13.2$ to $+4.3$; our unpublished data], Gyirong in the High Himalaya [ca. 499 Ma; $\varepsilon_{\text{Hf}}(t) = -13.9$ to -5.0 ; Wang et al., 2011], and the Baoshan Terrane [$\varepsilon_{\text{Hf}}(t) = -13.6$ to -10.2 ; Liu et al., 2009] (Fig. 7b).

6. Discussion

6.1. Early Paleozoic magmatism along the proto-Tethyan margin of Gondwana

The geochronological data reported here indicate that the metabasalts and silicic metavolcanic rocks from the southeast of Nyima were

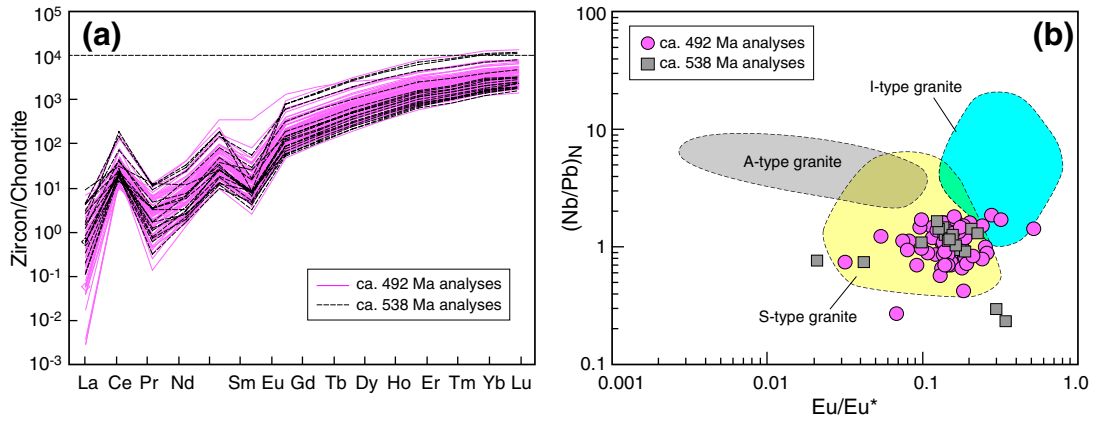


Fig. 4. (a) Chondrite-normalized REE patterns and (b) $(\text{Nb/Pb})_N$ versus Eu/Eu^* diagram for zircon grains from the silicic metavolcanic rocks in the central Lhasa subterrane. Fields of I-, S-, and A-type granites are from Wang et al. (2012).

formed synchronously at ca. 492 Ma, slightly postdating the Cambrian volcanism identified in eastern Xainza (ca. 501 Ma; Ji et al., 2009a) in the central Lhasa subterrane. Our data also reveal a probable magmatism of ca. 538 Ma in the study area. To the north of the Lhasa Terrane, coeval magmatic rocks have been identified by zircon U–Pb dating from the Amdo (ca. 531 Ma, Xu et al., 1985; ca. 488 Ma; Xie et al., 2010; ca. 532–470 Ma, Guynn et al., 2012; ca. 492 Ma, our unpublished data) and Western Qiangtang (476–471 Ma, Pullen et al., 2011) (Fig. 1b). To the south of the Lhasa Terrane, recent geochronological studies have reported the presence of coeval gneissic-granites from Gyirong (ca. 499 Ma; Wang et al., 2011) and Yadong (Shi et al., 2010) in the High Himalaya (Fig. 1b). These new age data, together with previously published zircon U–Pb age data (ca. 530–470 Ma)

from Tethyan, High, and Lesser Himalayas (cf. Miller et al., 2001; Cawood et al., 2007; Lee and Whitehouse, 2007; Quigley et al., 2008), suggest that the contemporaneous magmatism in the early Paleozoic was rather extensive in the present-day Tibetan Plateau and the Himalayas (Fig. 1b).

The early Paleozoic magmatism has also been recognized in other microcontinents along the proto-Tethyan margin of Gondwana. In central Iran (Fig. 1a), granitoids (including quartz diorite, granodiorite, and leucogranite) and volcanic rocks (including dacite and rhyodacite) have been dated using the zircon U–Pb method to be 547–522 Ma (Ramezani and Tucker, 2003; Hassanzadeh et al., 2008). Farther to the west, Ustaömer et al. (2009) reported two zircon U–Pb ages of 545.5 Ma and 531.4 Ma for granitic rocks from SE

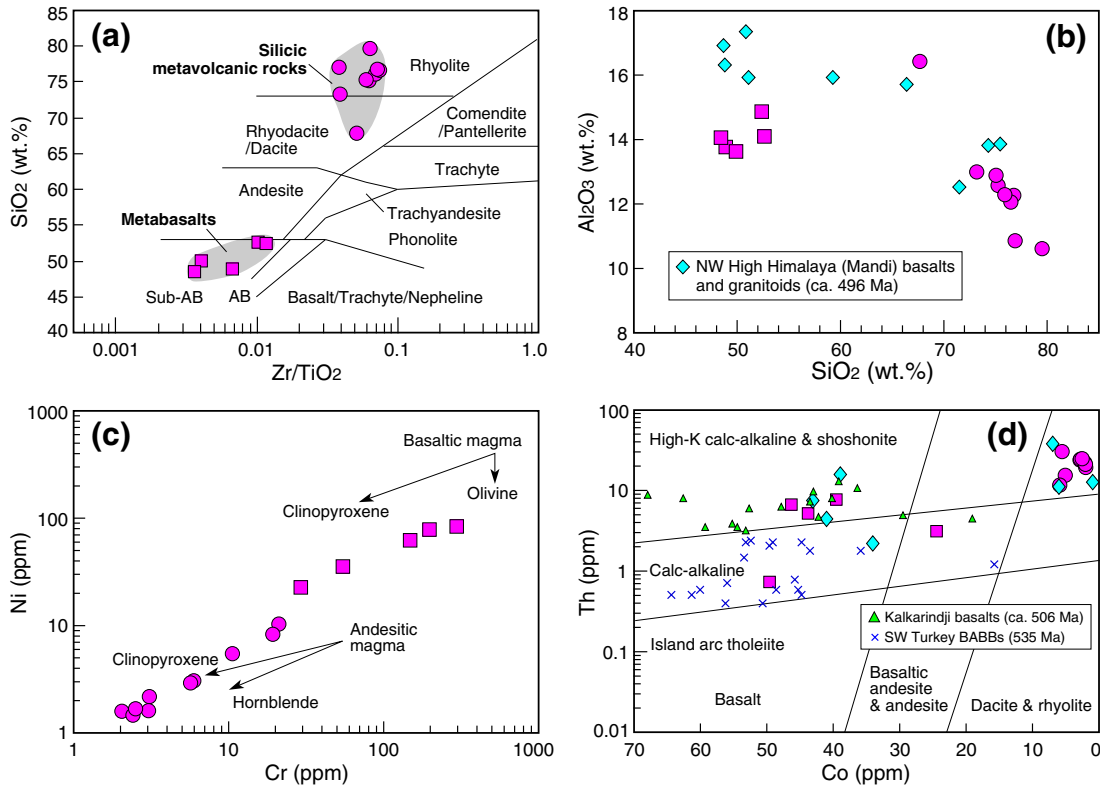


Fig. 5. Selected plots of the Cambrian metavolcanic rocks in the central Lhasa subterrane. (a) SiO_2 vs. Zr/TiO_2 diagram (Winchester and Floyd, 1977) for classification; (b) Al_2O_3 vs. SiO_2 plot; (c) Ni vs. Cr plot showing olivine- and clinopyroxene-dominated fractionation in the evolution of parental magmas to the metabasalts and hornblende-dominated fractionation in the silicic metavolcanic rocks. Partition coefficients are from Rollinson (1993); (d) Th vs. Co plot (Hastie et al., 2007) showing that the metavolcanic rocks were mostly high-K calc-alkaline. Data of Mandi magmatic rocks (Miller et al., 2001), back-arc basin basalts (BABBs) from SW Turkey (Gürsu and Göncüoğlu, 2005), and Kalkarindji basalts from present-day NW Australia (Glass and Phillips, 2006; Evins et al., 2009) are also plotted for comparison.

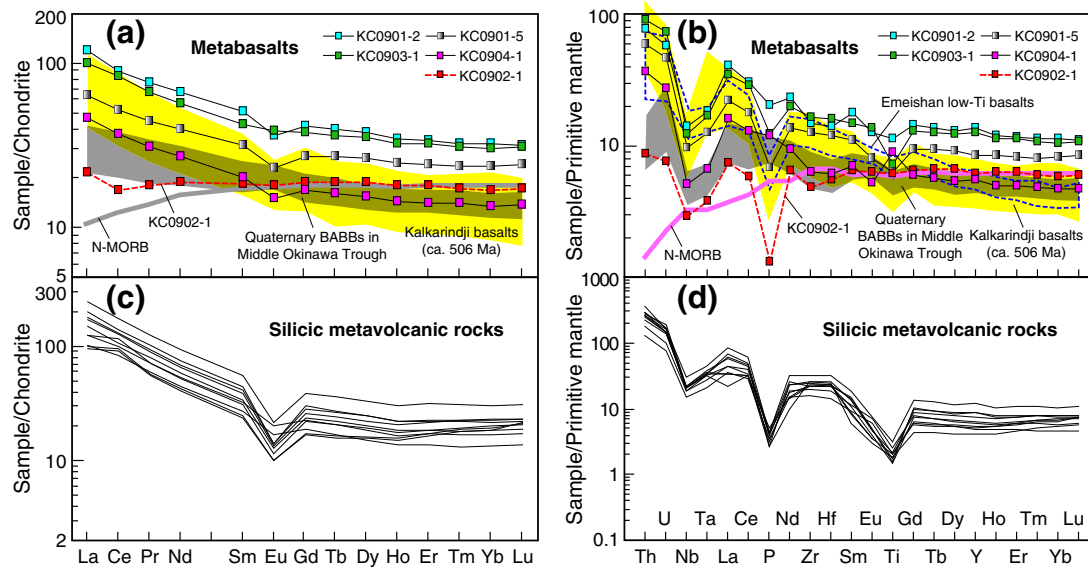


Fig. 6. Chondrite-normalized REE (a) and primitive-mantle-normalized trace element patterns (b) for the Cambrian metabasalts in the central Lhasa subterrane. N-MORB (Sun and McDonough, 1989), Quaternary BABBs from the Middle Okinawa Trough (Shinjo et al., 1999), Emeishan low-Ti basalts (Xiao et al., 2004), and Kalkarindji basalts (Glass and Phillips, 2006; Evins et al., 2009) are shown for comparison. Data for normalization and plotting are from Sun and McDonough (1989). Note that the Lhasa Cambrian metavolcanic rocks show different patterns from those of BABBs and Emeishan low-Ti basalts.

Turkey (Fig. 1a). To the east of the present-day Lhasa Terrane, contemporaneous early Paleozoic granitoids have been found in the Gongshan (ca. 487 Ma; Song et al., 2007), Tengchong (495–466 Ma; Chen et al., 2007), Baoshan (500–493 Ma; Liu et al., 2009) (Fig. 1a), northern Burma (ca. 491 Ma; Mitchell et al., in press), and Sibumasu (ca. 486 Ma; Metcalfe, 1998) terranes that are derived directly or indirectly from the Australian margin of eastern Gondwana (Metcalfe, 2009). Coeval early Paleozoic magmatism has not been documented in present-day NW Australia, possibly due to its poorly known late Cambrian to early Ordovician geology (Mory et al., 2003). Much farther east in present-day NE Australia, the available $^{40}\text{Ar}/^{39}\text{Ar}$ geochronological dates from basaltic rocks and zircon U–Pb dates from the associated dolerites indicate the occurrence of extensive mafic magmatism at ca. 513–505 Ma (Hanley and Wingate, 2000; Macdonald et al., 2005; Glass and Phillips, 2006; Evins et al., 2009). This mafic magmatism is known as the Kalkarindji continental flood basalt province (LIP) (cf. Glass and Phillips, 2006). Collectively, the currently available high-quality geochronological data reveal the

presence of coeval early Paleozoic magmatism along the proto-Tethyan margin of Gondwana, extending from Turkey and Iran to the present-day Tibetan Plateau, Himalayas, Tengchong, Baoshan (Fig. 1a), Burma, Sibumasu, and to NE Australia.

6.2. Tectonic setting of the Cambrian bimodal metavolcanic suite in the Lhasa Terrane

Field relationships, geochronological and geochemical data indicate that the Cambrian metavolcanic rocks in the central Lhasa subterrane are bimodal in character. As summarized by Pin and Paquette (1997), bimodal magmatic suites can occur in different geodynamic settings that can be identified by field occurrences and geochemical signatures of the mafic and silicic varieties. For example, bimodal magmatic suites from oceanic island arcs generally contain voluminous low-K tholeiitic mafic rocks and subordinate silicic rocks and display diagnostic geochemical signatures such as high $\varepsilon_{\text{Nd}}(t)$ values and strong Nb depletion (e.g., Ikeda and Yuasa, 1989).

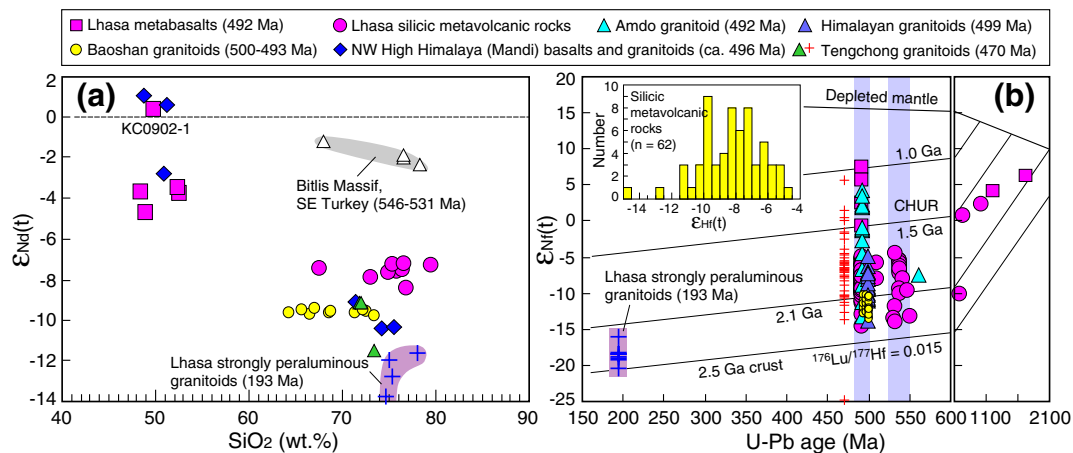


Fig. 7. Plots of whole-rock $\varepsilon_{\text{Nd}}(t)$ vs. SiO_2 (a) and $\varepsilon_{\text{Hf}}(t)$ vs. U–Pb ages (b) of the Cambrian metavolcanic rocks in the central Lhasa subterrane. Data of Amdo gneissic granite (ca. 492 Ma; our unpublished data), Himalayan gneissic granite (ca. 499 Ma; Wang et al., 2011), Baoshan granitoids (500–493 Ma; Liu et al., 2009), Tengchong granitoids (ca. 470 Ma; Chen et al., 2007), BABBs from Bitlis Massif, SE Turkey (546–531 Ma; Gürsu and Göncüoğlu, 2005), Mandi basalts and granitoids in the NW High Himalaya (ca. 496 Ma; Miller et al., 2001), and Lhasa strongly peraluminous granitoids (ca. 193 Ma; Zhu et al., 2011b) are shown for comparison. Inset in Fig. 7b shows histograms of $\varepsilon_{\text{Hf}}(t)$ zircons from the silicic metavolcanic rocks. See text for details.

Conversely, those from post-collisional to within-plate settings consist of mafic rocks that are generally tholeiitic and silicic rocks that generally display A-type signatures with high HFSE abundances (e.g., Hildreth et al., 1991; Pin and Paquette, 1997; Bonin, 2004; Shellnutt and Zhou, 2007; Zhu et al., 2007; Li et al., 2008a, 2008b; Zhang et al., 2008b). In contrast, bimodal magmatism linked to destructive plate margins is dominated by silicic rocks with the absence of alkaline affinities, which are generally associated with subordinate mafic rocks with high LILE/HFSE ratios (cf. Pin and Paquette, 1997).

In the case of the central Lhasa subterrane, sample KC0902-1 exhibited both MORB- (e.g., flat HFSE and HREE pattern) and arc-like (e.g.,

significant Th–U–La–Ce enrichment and Nb–Ta depletion) geochemical affinities (Figs. 6b and 8a) with a moderate Nb/Yb ratio. These features appear to suggest its formation in a back-arc basin or an oceanic island arc (Fig. 8b). However, we consider this interpretation unlikely because the other four metabasalt samples (1) were calc-alkaline (Fig. 5d) and displayed primitive mantle-normalized multi-element patterns significantly different from those of the back-arc basin basalts (BABBs) from the Middle Okinawa Trough (Fig. 6b) that developed on a continental basement (Shinjo et al., 1999), (2) plot in the volcanic arc basalt field (Fig. 8b, c and d) rather than straddle the volcanic arc basalt and MORB fields, as do the BABBs from the Middle Okinawa Trough

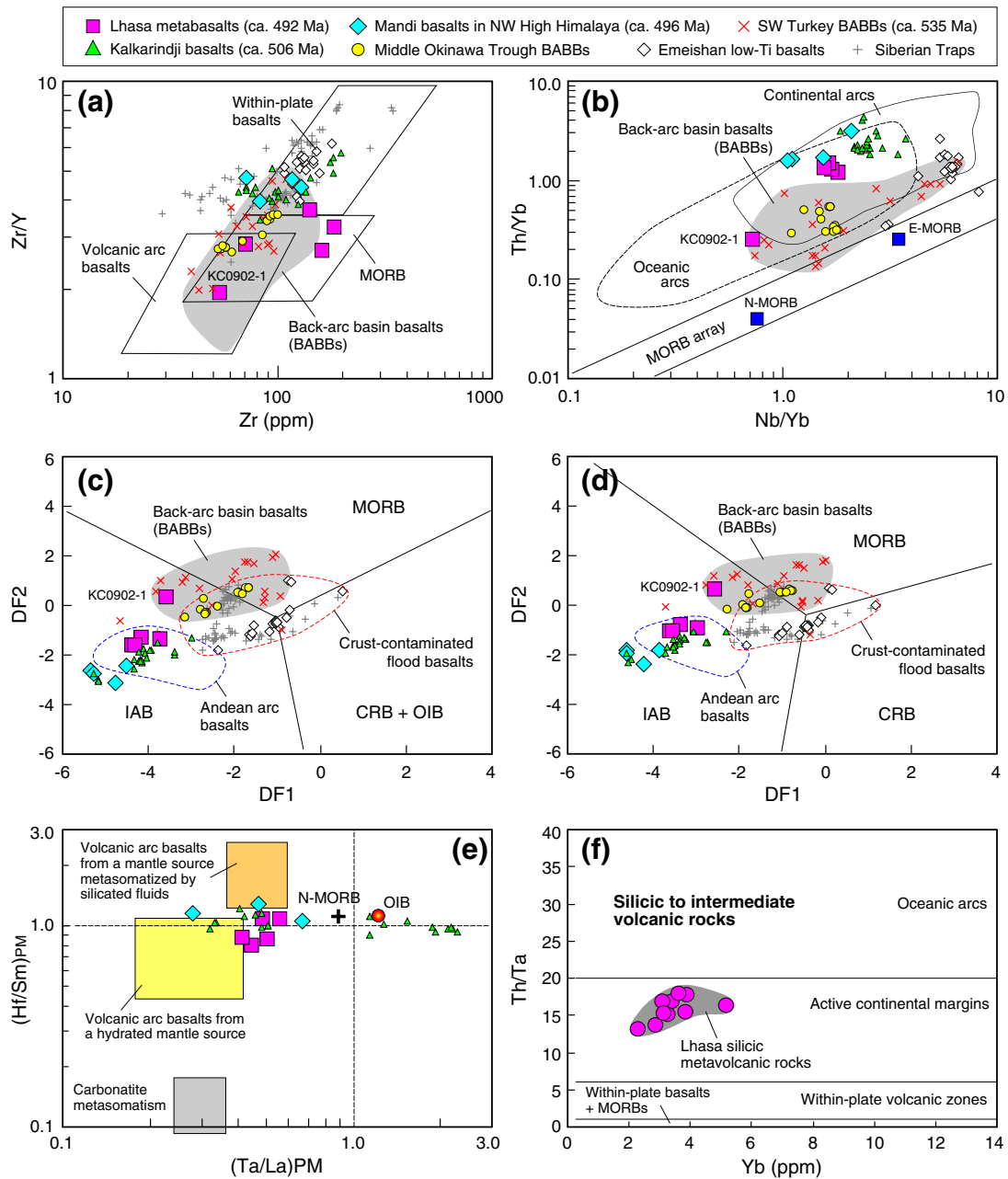


Fig. 8. Selected discrimination diagrams of the metabasalts in the Lhasa Terrane. (a) Zr/Y–Zr diagram (Pearce and Norry, 1979), back-arc basin basalts discrimination from Floyd et al. (1991); (b) Th/Yb–Nb/Yb (Pearce and Peate, 1995) diagrams showing the tectonic setting of the metabasalts; (c–d) IAB–MORB–CRB + OIB and IAB–MORB–CRB diagrams (Agrawal et al., 2008); (e) (Hf/Sm)_{PM}–(Ta/La)_{PM} diagram (La Flèche et al., 1998), where PM denotes normalization to the primitive mantle values of Sun and McDonough (1989); and (f) Th/Ta–Yb discriminant diagram for silicic to intermediate volcanic rocks (Gorton and Schandl, 2000). The fields of island arc (IAB), mid-ocean ridge (MORB), continental rift (CRB), and ocean-island (OIB) are from Agrawal et al. (2008).

Data sources: Mandi basalts in the NW High Himalaya (Miller et al., 2001), Kalkarindji basalts (Glass and Phillips, 2006; Evins et al., 2009), SW Turkey BABBs (Gürsu and Gönçüoğlu, 2005), Middle Okinawa Trough BABBs (Shinjo et al., 1999), Andean arc basalts (Hickey et al., 1986), Emeishan low-Ti basalts (Xiao et al., 2004), and Siberian Traps (<http://georoc.mpch-mainz.gwdg.de/georoc/Entry.html>).

(Shinjo et al., 1999) and SW Turkey (Gürsu and Göncüoğlu, 2005) on the immobile trace element discrimination diagrams of Agrawal et al. (2008), and (3) exhibited negative $\epsilon_{\text{Nd}}(t)$ values (-4.7 to -3.5 ; Table 1) that are inconsistent with oceanic island arc basalts with high $\epsilon_{\text{Nd}}(t)$ (Ikeda and Yuasa, 1989).

The metabasalt samples were characterized by significant negative Nb, Ta, Ti, Zr, and Hf anomalies relative to Th, U, and REEs in the primitive mantle-normalized multi-element patterns (Fig. 6b), similar to those of arc basalts (cf. Hickey et al., 1986). One possibility is that these rocks were emplaced at an active continental rift or a within-plate setting. This is because mafic rocks with arc signatures can also be observed in crust-contaminated continental flood basalts (CFBs) in continental rift or break-up settings, as exemplified by the Emeishan low-Ti basalts (Xiao et al., 2004) and Siberian Traps (Reichow et al., 2005). However, we consider that an active continental rift setting may not be suitable for their emplacement because (1) the metabasalt samples fall within the volcanic arc basalt field that closely resembles the Andean arc basalts erupted on a thick crust (cf. Hickey et al., 1986) rather than a within-plate (including continental rift and ocean-island) basalt field, as exemplified by the crust-contaminated Emeishan and Siberian CFBs (cf. Xiao et al., 2004; <http://georoc.mpch-mainz.gwdg.de/georoc/Entry.html>) on the immobile trace element discrimination diagrams (Fig. 8b, c, and d) (Pearce and Norry, 1979; Agrawal et al., 2008), and (2) the silicic metavolcanic rocks were low in HFSE abundances (e.g., Nb = 10.6–21.2 ppm; Zr = 175–362 ppm) and had low $10,000 \times \text{Ga/Al}$ ratios (1.41–2.49), significantly distinctive from the silicic rocks with high HFSE abundances in continental rift or within-plate settings (cf. Whalen et al., 1987; Pin and Paquette, 1997; Zhu et al., 2007; Li et al., 2008a, 2008b; Zhang et al., 2008b).

Another possibility, which we prefer, is that the arc signatures of the metabasalts were associated with subduction-related processes. Several lines of evidence support this possibility. First, the metabasalts were geochemically similar to the volcanic arc basalts in terms of the immobile trace element discrimination diagrams of Pearce and Norry (1979) (Fig. 8a and b) and Agrawal et al. (2008) (Fig. 8c and d). Second, the metabasalt samples plot along the trajectory between N-MORB and volcanic arc basalts from a hydrated mantle source in the $(\text{Hf/Sm})_{\text{PM}}$ vs. $(\text{Th/Ta})_{\text{PM}}$ diagram (Fig. 8e; La Flèche et al., 1998), indicating that the source region of the metabasalts has been metasomatized by subduction-related fluids (La Flèche et al., 1998; Li et al., 2009). Third, the silicic metavolcanic samples had Th/Ta ratios of 13.2–17.9 and plot in the active continental margin field on the Th/Ta vs. Yb diagram (Gorton and Schandl, 2000; Fig. 8f).

Given the poor understanding of Cambrian geology of the central Lhasa subterrane, the geochemical signatures and the discussions above, in combination with the predominance of silicic metavolcanic rocks and the presence of shallow-water sedimentary records (e.g., quartzite interlayers with graded and cross-beddings, Ji et al., 2009a; Li et al., 2010), enable us to propose that the Cambrian bimodal metavolcanic suite in the central Lhasa subterrane was developed in an Andean-type active continental margin rather than a continental rift (or within-plate), back-arc, or oceanic arc setting. Bimodal magmatic rocks formed in active or recently active subduction zone environments analogous to the proposed setting for the Cambrian bimodal metavolcanic rocks in the central Lhasa subterrane are also known from the Paleoproterozoic Green Mountain arc in Colorado (Jones et al., 2011), Jurassic Mudurnu arc in northern Turkey (Genç and Tüysüz, 2010), early Cretaceous magmatic arc in the northern Lhasa subterrane (Sui et al., 2010), Cretaceous Greater Antilles arc in Puerto Rico (Jolly et al., 2008), and modern Tonga–Kermadec arc in the southwest Pacific (e.g., Smith et al., 2006).

6.3. Petrogenesis of the Cambrian metavolcanic rocks in the Lhasa Terrane

6.3.1. Metabasaltic rocks

The Cambrian metabasaltic rocks were characterized by low Mg# (34–55) and low Cr and Ni abundances, suggesting that the mantle-

derived melts parental to these rocks must have experienced significant fractional crystallization of olivine and clinopyroxene (Fig. 5c). The absence of a negative correlation between Al_2O_3 and SiO_2 (Fig. 5b) and the slightly negative Eu anomalies of the metabasalts (Fig. 6a) indicate a limited fractionation of plagioclase.

Generally, the arc signatures and negative $\epsilon_{\text{Nd}}(t)$ values observed in the metabasaltic rocks can be accounted for by either the involvement of an enriched mantle source component or significant crustal contamination of an asthenospheric melt. It is noteworthy that the four metabasalt samples (except sample KC0902-1) were characterized by subparallel incompatible trace element patterns (Fig. 6a and b) and a restricted $\epsilon_{\text{Nd}}(t)$ range (-4.7 to -3.5 ; Table 1), although they displayed relatively large variations in trace element compositions. These features, together with the lack of correlation between $\epsilon_{\text{Nd}}(t)$ values and SiO_2 contents (Fig. 7a), indicate that crustal assimilation was insignificant in the genesis of the metabasalts. In this case, the arc signatures, high-K calc-alkaline character (Fig. 5d), negative $\epsilon_{\text{Nd}}(t)$, and low zircon $\epsilon_{\text{Hf}}(t)$ (-0.7 to $+7.5$; Table 2) for these rocks can best be interpreted as a result of varying degrees of partial melting of an enriched lithospheric mantle that was metasomatized by subduction-derived components (including hydrous fluids and melts of subducted continental material) (Bonin, 2004; Clift et al., 2009). This interpretation is analogous to the origin proposed for the high-K calc-alkaline suites with similar isotopic compositions worldwide (cf. Bonin, 2004; Zhang et al., 2011).

In contrast, sample KC0902-1 was calc-alkaline in nature (Fig. 5d) and showed distinct elemental (Fig. 6a and b) and isotopic compositions (Fig. 7a), e.g., high MgO (8.12%) and Cr (296 ppm), a flat REE pattern, and elevated $\epsilon_{\text{Nd}}(t)$ ($+0.3$) values relative to the other four metabasalt samples. Such geochemical variations, observed in a single locality, cannot be attributed to an origin from a common parental magma shared by the other four samples. Instead, the compositional variations documented by the metabasaltic rocks in the central Lhasa subterrane are most likely associated with a heterogeneous mantle source (with large contributions from asthenospheric mantle for the origin of sample KC0902-1) that was modified by subduction-related components. Similar geochemical variations have also been observed in basalts from the Southern Okinawa Trough by Shinjo et al. (1999), who suggested that the compositional variation is more likely to have been inherited from a heterogeneous mantle source caused by subduction processes.

6.3.2. Silicic metavolcanic rocks

Two types of processes have been proposed for the origin of the silicic end-member in the bimodal magmatic suite, including (1) extensive fractional crystallization from a common mantle-derived magma parental to the mafic end-member, coupled with crustal contamination (cf. Pin and Paquette, 1997; Bonin, 2004; Genç and Tüysüz, 2010, and the references therein), and (2) crustal anatexis caused by mantle-derived mafic magma with distinct isotopic compositions (cf. Shellnutt and Zhou, 2007; Zhu et al., 2007; Jones, et al., 2011). In the case of the silicic metavolcanic rocks from the central Lhasa subterrane, the lack of a negative correlation defined by Al_2O_3 vs. SiO_2 (Fig. 5b) and the distinct differences documented by the whole-rock $\epsilon_{\text{Nd}}(t)$ and zircon $\epsilon_{\text{Hf}}(t)$ values between the metabasalts and silicic rocks (Fig. 7a and b) indicate that the silicic rocks could not have been produced by fractional crystallization (or plus assimilation) of the coeval metabasalts.

The silicic metavolcanic rocks in the central Lhasa subterrane had high SiO_2 (68–80 wt.%) and negative $\epsilon_{\text{Nd}}(t)$ values (-8.4 to -7.2) that were significantly different from those of the metabasalts (Table 1). These features, together with the negative zircon $\epsilon_{\text{Hf}}(t)$ values (-14.7 to -4.8), indicate that the silicic metavolcanic rocks were derived from anatexis of the ancient basement of the Lhasa microcontinent. Taking into account their exclusively negative $\epsilon_{\text{Nd}}(t)$ (Table 1), zircon $\epsilon_{\text{Hf}}(t)$ (Table 2), and zircon trace element

compositions (Fig. 4b), these silicic metavolcanic rocks are considered to be equivalents of S-type granites (rather than A-type granites) with mature crustal protoliths.

It is noteworthy that the silicic metavolcanic rocks had significantly higher whole-rock $\varepsilon_{\text{Nd}}(t)$ and zircon $\varepsilon_{\text{Hf}}(t)$ values than those of the strongly peraluminous early Jurassic granites [$\varepsilon_{\text{Nd}}(t) = -14.1$ to -11.1 , Liu et al., 2006; $\varepsilon_{\text{Hf}}(t) = -20.5$ to -16.0 , Zhu et al., 2011b] in the central Lhasa subterrane (Fig. 7a and b). It follows that the silicic metavolcanic rocks are not pure crustal melts but are rather hybrid melts with contributions from mantle-derived components. The large $\varepsilon_{\text{Hf}}(t)$ variation of the 492 Ma zircons, which mostly range from -10 to -5 with some “outlier” analyses that exhibit strongly negative $\varepsilon_{\text{Hf}}(t)$ values as low as -14.7 (see inset in Fig. 7b), further corroborate that mantle-derived components have been introduced into the parental magmas of the silicic metavolcanic rocks (cf. Kemp and Hawkesworth, 2006; Kemp et al., 2007; Yang et al., 2007; Zhu et al., 2011b). Therefore, the Cambrian silicic metavolcanic rocks in the central Lhasa subterrane can be interpreted as resulting from the mixing of Lhasa basement-derived melts with minor mantle-derived basaltic melts.

6.4. Tectonic implications

6.4.1. An early Paleozoic Andean-type magmatic arc along the Australian proto-Tethyan margin

The Tethyan, High, and Lesser Himalayas were previously considered to be parts of the passive margin of the northern Indian

continent from the Precambrian to Cretaceous times (Brookfield, 1993). However, this inferred Precambrian to early Paleozoic passive margin scenario is inconsistent with the emplacement of numerous Early Paleozoic granites in the Himalayas (Fig. 1b) (see above). Miller et al. (2001) argued in support of Debon et al. (1986) and Le Fort et al. (1986) that the extensive magmatism was emplaced in an extensional setting rather than a subduction- to collision-related setting by mainly considering (1) the absence of distinctive spikes of Sr and Ba (that are more or less mobilized during metamorphism and alteration) observed in the Mandi basalts (ca. 496 Ma) from the NW High Himalaya (Fig. 1b), (2) the short-lasting magmatism from 550 to 470 Ma, and (3) the absence of the Cambro–Ordovician metamorphic and deformation records in the Himalayas. However, subsequent field and geochronological data indicated that at least the Kathmandu region in the High Himalaya underwent deformation during the 500–475 Ma (Gehrels et al., 2006; Cawood et al., 2007), although the Indian proto-Tethyan margin has been strongly affected by the Cenozoic Himalayan tectonothermal events. Cawood and Buchan (2007) and Cawood et al. (2007) argued that the termination of subduction zones within the assembling Gondwana supercontinent that occurred between 570 and 510 Ma had to be compensated for by the initiation of subduction zones along the Gondwana Pacific and proto-Tethyan margins. From this global geodynamic perspective, Cawood et al. (2007) interpreted the extensive early Paleozoic magmatism and coeval metamorphism and deformation in the Himalayas as being related to either ongoing subduction of the proto-Tethyan Ocean lithosphere beneath the northern Indian continent or the accretion

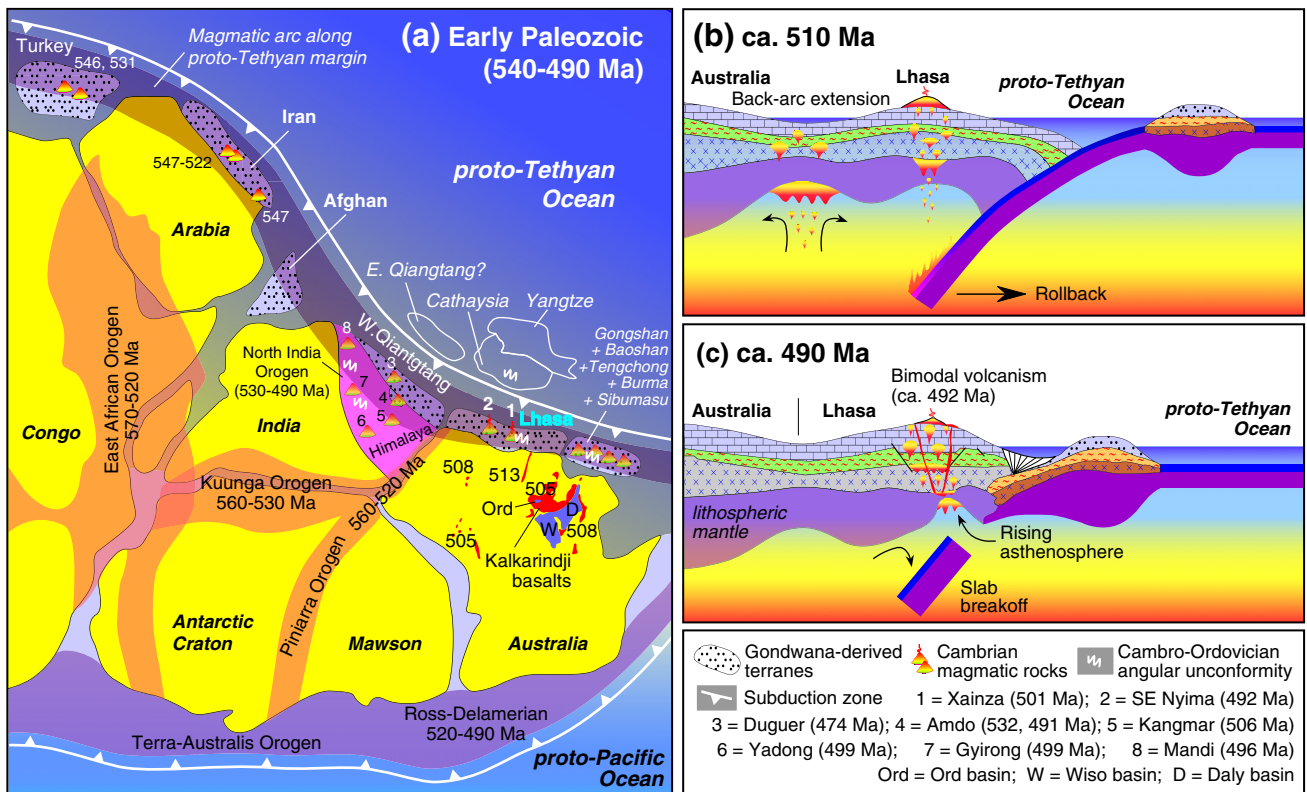


Fig. 9. (a) Reconstruction of the India–Australia proto-Tethyan margin (modified from Kusky et al., 2003; Cawood et al., 2007) showing the location of the proposed early Paleozoic Andean-type magmatic arc from the Western Qiangtang, Amdo, and Tethyan Himalaya situated in the Indian proto-Tethyan margin, to Lhasa and other possible microcontinents (e.g., Gongshan, Baoshan, Tengchong, and Sibumasu) paleogeographically located in the Australian proto-Tethyan margin. Paleogeographical positions: the locations of the Lhasa Terrane (Zhu et al., 2011a), South China (including Yangtze and Cathaysia) (Wang et al. 2010), Kalkarindji basalts with ages (Glass and Phillips, 2006), and Ord, Wiso, and Daly basins (Lindsay et al., 2005). The general arrangement of the Gongshan, Baoshan, Tengchong, Burma, and Sibumasu was tentatively inferred from Metcalfe (2009) and this study based on the tectonomagmatic data reported by Chen et al. (2007), Huang et al. (2009), Liu et al. (2009), Song et al. (2010), and Mitchell et al. (in press). Note that the Cambro–Ordovician angular unconformity is developed in the eastern Cathaysia, while magmatic rocks with an age range of 510–470 Ma are not known to exist in South China (Wang et al., 2010, and references therein). (b–c) Schematic illustrations showing the geodynamic evolution of the Lhasa Terrane during the early Paleozoic. Note that the rollback of the proto-Tethyan Ocean lithosphere at ca. 510 Ma and subsequent slab break-off at ca. 492 Ma may have led to the extensive emplacement of magmatism in a broad back-arc region and to the generation of the bimodal volcanism within the magmatic arc, respectively.

of microcontinental slivers represented by the central Lhasa subterrane and Qiangtang Terrane. Similar Andean-type orogenic activity has also been proposed for the Precambrian–early Paleozoic magmatism along the margins of Arabia, central Iran, and SW Turkey (Fig. 9a) (Ramezani and Tucker, 2003; Hassanzadeh et al., 2008; Horton et al., 2008; Saki, 2010; Mahmoud et al., 2011).

If the Indian proto-Tethyan margin underwent an Andean-type subduction and associated orogenic event (Cawood et al., 2007), the adjoining Australian proto-Tethyan margin must have experienced comparable tectonomagmatic events, as did the adjoining Iranian, Arabian, and Turkey margins (Fig. 9a) (Ramezani and Tucker, 2003; Hassanzadeh et al., 2008; Horton et al., 2008; Saki, 2010; Mahmoud et al., 2011). However, a record of such tectonomagmatic events is lacking in the present-day NW Australian continent (cf. Mory et al., 2003; Cawood et al., 2007). An integrated study on detrital zircon U–Pb chronology, Hf isotope geochemistry, and provenance discrimination for Paleozoic metasedimentary rocks in the Lhasa, Qiangtang, and Tethyan Himalayan terranes has shown that the Lhasa Terrane may have originated from the Australian Gondwana (Zhu et al., 2011a, 2012) as originally proposed by Audley-Charles (1983, 1984, 1988) rather than the Indian Gondwana as traditionally thought (cf. Sengör, 1987; Yin and Harrison, 2000; Pan et al., 2004; Metcalfe, 2006, 2009). The coeval Precambrian metamorphism recently recognized in both the central Lhasa subterrane (ca. 720 Ma; Zhang et al., 2010) and northern Australia (i.e. the ~750–720 Ma Miles Orogeny; Bagas, 2004) further corroborates the paleogeographical connection between them because the coeval metamorphic record is lacking in the Himalayas and the interior Indian continent (cf. Zhu et al., 2012). In this case, the Andean-type magmatism documented by the Cambrian bimodal metavolcanic rocks in SE Nyima (this study) and the metarhyolites in Xainza (Ji et al., 2009a) in the central Lhasa subterrane (Fig. 1b) can best be interpreted as recording an Andean-type magmatic arc along the Australian proto-Tethyan margin (Fig. 9a).

The presence of extensive mafic magmatism at ca. 513–505 Ma (i.e., the Kalkarindji LIP) (Hanley and Wingate, 2000; Macdonald et al., 2005; Glass and Phillips, 2006; Evins et al., 2009) in present-day NE Australia (Fig. 9a) seems to be at odds with the proposed Andean-type magmatic arc along the Australian proto-Tethyan margin. However, it should be noted that the proposed Andean-type magmatic arc is located outboard of present-day NE Australia, as indicated by the presence of coeval early Paleozoic granitoids with similar isotopic compositions to the High Himalaya (Wang et al., 2011) and central Lhasa subterrane (this study) (Fig. 7a and b) observed in the Tengchong (Chen et al., 2007), Baoshan (Liu et al., 2009), and Burma (Mitchell et al., in press) terranes, all of which were derived from the Australian margin, as inferred from stratigraphical and biogeographical data (Wang et al., 2001; Ueno, 2003; Metcalfe, 2009). A recent study on magmatism and detrital zircon ages indicated that the Gongshan Terrane (Fig. 9a) may have been an eastern extension of the Lhasa Terrane (Song et al., 2010). In such cases, the extensive Kalkarindji mafic magmatism can be interpreted as having been emplaced in a broad back-arc region, similar to the Himalayas (Cawood et al., 2007). This is supported by (1) its subduction-related geochemical (e.g., strong negative Nb–Ti–P anomalies seen in Fig. 6b of this study and Fig. 2 of Glass and Phillips, 2006) and island-arc basalt affinities (Fig. 8c and d) coupled with relatively high Zr/Y ratios (Fig. 8b), (2) its across-strike width (ca. 700 km; Glass and Phillips, 2006) comparable to the pre-Cenozoic across-strike width of the Himalayan granite belts (ca. 700 km; Cawood et al., 2007) (Fig. 9a), and (3) the onset of subsidence of associated intracratonic basins (e.g., Ord, Daly, and Wiso basins) located in present-day NE Australia (Fig. 9a) in the early Paleozoic (Lindsay et al., 2005). Our re-interpretation for the generation of the Kalkarindji mafic magmatism is analogous to the origin of the Neoproterozoic magmatism in South China (Zhao et al., 2011), where the rifting and related

magmatism have been re-interpreted to be associated with subduction-related back-arc spreading.

Considering the fact that the ~492 Ma gneissic granite from Amdo showed negative to positive zircon $\varepsilon_{\text{Hf}}(t)$ values (–13.2 to +4.3) (our unpublished data), which indicate larger contributions of mantle-derived components relative to the coeval S-type granitic gneiss with mature crustal protoliths [$\varepsilon_{\text{Hf}}(t) = -13.9$ to -5.0 ; Wang et al., 2011] in the High Himalaya (Fig. 7b), and that the Kangmar granites in the Tethyan Himalaya (Fig. 1b) are intruded by the gabbroic dykes (ca. 480 Ma; Zhao, personal communication, 2011), which can be considered as mafic end-member equivalents to the metabasalts in the central Lhasa subterrane, we propose that the Western Qiangtang–Amdo–Tethyan Himalaya situated in the Indian proto-Tethyan margin and the Lhasa Terrane and other possible microcontinents or terranes with coeval magmatism (e.g., Gongshan, Baoshan, Tengchong, Burma, and Sibumasu) located in the Australian proto-Tethyan margin (Fig. 9a) represent an early Paleozoic Andean-type magmatic arc facing the proto-Tethyan Ocean.

6.4.2. A favored subduction–back arc extension and slab break-off model for the early Paleozoic tectonomagmatism along the India–Australia proto-Tethyan margin

Our interpretation and the supporting new data confirm the previous recognition that the early Paleozoic magmatic arc was situated in, or north of, the Tethyan Himalaya (cf. Cawood et al., 2007). The Cambro–Ordovician angular unconformity has been observed not only in the Tethyan Himalaya in the northern Indian continent (cf. Garzanti et al., 1986; Baig et al., 1988; Pan et al., 2004; Myrow et al., 2006) but also in the Lhasa (Li et al., 2010), Baoshan (Huang et al., 2009), and possibly in Burma (cf. Mitchell et al., in press) terranes in the northern Australian continent (Fig. 9a). Considering the presence of the Cambrian continental-arc magmatic products recognized in both the Lhasa (Ji et al., 2009a; this study), Baoshan (Liu et al., 2009), and Burma (cf. Mitchell et al., in press) terranes, it is evident that both the continental-arc magmatism and the angular unconformity were developed in the same geotectonic location. In addition, field relationships and geochronological data indicate that the bimodal magmatism predated the development of the Cambro–Ordovician angular unconformity in the central Lhasa subterrane (Li et al., 2010; this study). These observations are highly analogous to the Cretaceous tectonomagmatic events in the northern Lhasa subterrane, where the early Cretaceous arc magmatism (131–115 Ma), bimodal magmatism (ca. 110 Ma; Sui et al., 2010), and angular unconformity between the Upper Cretaceous and underlying strata (cf. Kapp et al., 2005b, 2007; Pan et al., 2006) have been associated with subduction, slab break-off of the Bangong–Nujiang Ocean lithosphere, and final Lhasa–Qiangtang amalgamation (cf. Zhu et al., 2009a, 2011b). Although it remains difficult to explore the geodynamic mechanism responsible for generation of the Cambrian bimodal volcanic rocks in the central Lhasa subterrane because of the poorly-preserved Cambro–Ordovician geological records, these comparable tectonomagmatic events lead us to argue that the slab break-off was a plausible mechanism (Cawood et al., 2007) that triggered emplacement of the magmatism at ~492 Ma following collisional accretion of terranes or microcontinents (possibly Eastern Qiangtang and South China). This is also because the slab break-off in subduction–collision systems may cause a short-lived extensional setting within the overriding plate due to the asthenospheric upwelling (cf. Davies and von Blanckenburg, 1995; Duret et al., 2011) required for generation of the bimodal magmatism that was likely emplaced in an extensional setting. In this case, the early Paleozoic tectonomagmatic evolution along the India–Australia proto-Tethyan margin can be described by a subduction–back arc extension–slab break-off model as follows (Fig. 9b and c).

The Andean-type magmatism was likely active by ca. 530 Ma along the Australian proto-Tethyan margin, as indicated by the presence of ca. 538 Ma inherited zircon grains in silicic metavolcanic rocks in the

central Lhasa subterrane (Fig. 3). With continued subduction of the proto-Tethyan Ocean lithosphere, gravitational sinking led to slab retreat at ca. 510 Ma (Fig. 9b). This rollback would have then led to back-arc extension and asthenospheric upwelling. As a result, the subduction-induced decompression mantle melting would lead to the generation of widespread basaltic volcanism with arc- and within-plate-like geochemical signatures (Saunders and Tarney, 1984) in a broad back-arc region. This volcanism is represented by the extensive Kalkarindji volcanic field in present-day NE Australia and the Mandi basalts in the NW High Himalaya (Fig. 8). The decompression mantle melting may have also triggered crustal anatexis to produce voluminous granites, as observed in the High and Lesser Himalayas (cf. Cawood et al., 2007). Subsequently, the slab break-off of the subducting proto-Tethyan Ocean lithosphere may have occurred at ca. 492 Ma (Fig. 9c), following collisional accretion of microcontinents or terranes (Cawood et al., 2007) located outboard of the magmatic arc (e.g., Eastern Qiangtang and South China), ultimately creating the Cambro–Ordovician orogeny in the Tethyan Himalaya (Gehrels et al., 2003), Lhasa, Burma, and Baoshan terranes. This inferred slab break-off resulted in partial melting of the metasomatized lithosphere mantle, producing the high-K calc-alkaline basaltic melts parental to the metabasalts in the central Lhasa subterrane. Such mantle-derived magmas may have also provided the heat and material for deep crustal anatexis, leading to the production of silicic melts of isotopically hybrid compositions, as seen in the silicic metavolcanic rocks in the central Lhasa subterrane and the granitoids in the Amdo region.

Alternatively, lithospheric delamination can be considered as another possible mechanism to explain the generation of the 492-Ma bimodal suite in the central Lhasa subterrane. However, we tentatively discard this possibility because the Cambro–Ordovician angular unconformity along the India–Australia proto-Tethyan margin (Fig. 9a) and associated field and geochronological data indicate that the possible lithospheric stacking or crustal thickening along this margin occurred ca. 500–475 Ma (cf. Gehrels et al., 2006; Cawood et al., 2007), which is coeval with or postdates the Cambrian bimodal magmatism identified in the central Lhasa subterrane. This is not the case for lithospheric delamination that requires preexisting lithospheric stacking or crustal thickening (cf. Kay and Kay, 1993; Bonin, 2004; Chung et al., 2005, 2009). Nevertheless, we note that our favored model is proposed largely based on the limited data currently available for the Cambrian geology in the Lhasa Terrane and northern Australia. Further investigations and more data on the Cambrian geological records are required for further testing of our explanations pertaining to the geodynamic mechanism involved in the generation of the Cambrian bimodal magmatism identified in the central Lhasa subterrane.

7. Conclusions

- 1) The metabasalts and silicic metavolcanic rocks in the central Lhasa subterrane were synchronously emplaced approximately 492 Ma, forming a bimodal volcanic suite.
- 2) Metabasaltic rocks were derived from partial melting of an enriched lithospheric mantle source that was metasomatized by subduction events. Magmas derived from this source underwent significant fractional crystallization of olivine and clinopyroxene. Silicic metavolcanic rocks were the products of partial melting of the ancient Lhasa basement with minor mafic magma contributions.
- 3) The Cambrian bimodal metavolcanic rocks in the central Lhasa subterrane were most likely emplaced at an Andean-type active margin and represent an early Paleozoic Andean-type magmatic arc paleogeographically located in the Australian proto-Tethyan margin.
- 4) The generation of these bimodal metavolcanic rocks may be a result of slab break-off related heat and asthenospheric material flux following the accretion of microcontinents or terranes (e.g., Eastern Qiangtang and South China) located outboard of the Andean continental margin.

Supplementary materials related to this article can be found online at [doi:10.1016/j.chemgeo.2011.12.024](https://doi.org/10.1016/j.chemgeo.2011.12.024).

Acknowledgments

This research was financially co-supported by the National Key Project for Basic Research of China (Project 2009CB421002, 2011CB403102, and 2012CB822001), the Chinese National Natural Science Foundation (41073013, 40830317, and 40973026), the Fundamental Research Funds for the Central Universities (2010ZD02), the New Century Excellent Talents in University (NCET-10-0711), the Program for Changjiang Scholars and Innovative Research Team in University of Ministry of Education of China (PCSIRT), and the Programme of the China Geological Survey (1212011121260 and 1212011121066). We thank Peter Clift, one anonymous reviewer, and Sun-Lin Chung (guest editor) for constructive comments that have improved the quality of this paper and Editor Klaus Mezger for comments and editorial handling. We also thank Zhao-Chu Hu and Meng-Ning Dai for helping with LA-ICP-MS U–Pb and Lu–Hf isotopic analyses and Shao-Long Mo, Hai-Hong Chen, Qing-Song Chang, Fan-Yi Meng, and Dan Sheng for helping with whole-rock geochemical analysis. Yaoling Niu thanks the Leverhulme Trust for a Research Fellowship and Durham University for a Christopherson/Knott Fellowship. Yildirim Dilek's work in Tibet was supported by the China University of Geosciences (Beijing) and Miami University Distinguished Professor discretionary funds.

References

- Agrawal, S., Guevara, M., Verma, S.P., 2008. Tectonic discrimination of basic and ultrabasic rocks through log-transformed ratios of immobile trace elements. *International Geology Review* 50, 1057–1079.
- Allègre, C.J., Courtillot, V., Tapponnier, P., other 32 co-authors, 1984. Structure and evolution of the Himalaya–Tibet orogenic belt. *Nature* 307, 17–22.
- Andersen, T., 2002. Correction of common lead in U–Pb analyses that do not report ^{204}Pb . *Chemical Geology* 192, 59–79.
- Audley-Charles, M.G., 1983. Reconstruction of eastern Gondwanaland. *Nature* 306, 48–50.
- Audley-Charles, M.G., 1984. Cold Gondwana, warm Tethys and the Tibetan Lhasa block. *Nature* 310, 165–166.
- Audley-Charles, M.G., 1988. Evolution of the southern margin of Tethys (North Australian region) from early Permian to late Cretaceous. *Geological Society Special Publication* 37, 79–100.
- Bagas, L., 2004. Proterozoic evolution and tectonic setting of the northwest Paterson Orogen, Western Australia. *Precambrian Research* 128, 475–496.
- Baig, M.S., Lawrence, R.D., Snee, L.W., 1988. Evidence for late Precambrian to early Cambrian orogeny in northwest Himalaya, Pakistan. *Geological Magazine* 125, 83–86.
- Bonin, B., 2004. Do coeval mafic and felsic magmas in post-collisional to within-plate regimes necessarily imply two contrasting, mantle and crustal, sources? A review. *Lithos* 78, 1–24.
- Bouvier, A., Vervoort, J.D., Patchett, P.J., 2008. The Lu–Hf and Sm–Nd isotopic composition of CHUR: constraints from unequilibrated chondrites and implications for the bulk composition of terrestrial planets. *Earth and Planetary Science Letters* 273, 48–57.
- Brookfield, M.E., 1993. The Himalaya passive margin from Precambrian to Cretaceous times. *Sedimentary Geology* 84, 1–35.
- Cawood, P.A., Buchan, C., 2007. Linking accretionary orogenesis with supercontinent assembly. *Earth-Science Reviews* 82, 217–256.
- Cawood, P.A., Johnson, M.R.W., Nemchin, A.A., 2007. Early Palaeozoic orogenesis along the Indian margin of Gondwana: tectonic response to Gondwana assembly. *Earth and Planetary Science Letters* 255, 70–84.
- Chen, F.K., Li, X.H., Wang, X.L., Li, Q.L., Siebel, W., 2007. Zircon age and Nd–Hf isotopic composition of the Yunnan Tethyan belt, southwestern China. *International Journal of Earth Sciences* 96, 1179–1194.
- Chung, S.L., Chu, M.F., Zhang, Y.Q., Xie, Y.W., Lo, C.H., Lee, T.Y., Lan, C.Y., Li, X.H., Zhang, Q., Wang, Y.Z., 2005. Tibetan tectonic evolution inferred from spatial and temporal variations in post-collisional magmatism. *Earth-Science Reviews* 68, 173–196.
- Chung, S.L., Chu, M.F., Ji, J.Q., O'Reilly, S.Y., Pearson, N.J., Liu, D.Y., Lee, T.Y., Lo, C.H., 2009. The nature and timing of crustal thickening in Southern Tibet: geochemical and zircon Hf isotopic constraints from postcollisional adakites. *Tectonophysics* 477, 36–48.
- Clift, P., Vannucchi, P., Phipps, Morgan J., 2009. Crustal redistribution, crust–mantle recycling and Phanerozoic evolution of the continental crust. *Earth-Science Reviews* 97, 80–104.
- Collins, A.S., Pisarevsky, S., 2005. Amalgamating eastern Gondwana: the evolution of the circum-Indian orogens. *Earth-Science Reviews* 71, 229–270.

- Davies, J.H., von Blanckenburg, F., 1995. Slab breakoff: a model of lithospheric detachment and its test in the magmatism and deformation of collisional orogens. *Earth and Planetary Science Letters* 129, 85–102.
- Debon, F., Le Fort, P., Sheppard, S.M.F., Sonet, J., 1986. The four plutonic belts of the Trans-Himalaya–Himalaya: a chemical, mineralogical, isotopic and chronological synthesis along a Tibet–Nepal section. *Journal of Petrology* 27, 219–250.
- Dewey, J.F., Shackleton, R.M., Chang, C.F., Sun, Y.Y., 1988. The tectonic evolution of the Tibetan Plateau. *Philosophical Transactions of the Royal Society of London (Series A): Mathematical and Physical Sciences* 327, 379–413.
- Dong, X., Zhang, Z.M., Liu, F., Wang, W., Yu, F., Shen, K., 2011a. Zircon U–Pb geochronology of the Nyainqentanglha Group from the Lhasa terrane: new constraints on the Triassic orogeny of the south Tibet. *Journal of Asian Earth Sciences*. doi:10.1016/j.jseas.2011.01.014.
- Dong, X., Zhang, Z.M., Santosh, M., Wang, W., Yu, F., Liu, F., 2011b. Late Neoproterozoic thermal events in the northern Lhasa terrane, south Tibet: zircon chronology and tectonic implications. *Journal of Geodynamics*. doi:10.1016/j.jog.2011.05.002.
- Duret, T., Gerya, T.V., May, D.A., 2011. Numerical modelling of spontaneous slab breakoff and subsequent topographic response. *Tectonophysics* 502, 244–256.
- Evens, L.Z., Jourdan, F., Phillips, D., 2009. The Cambrian Kalkarindji Large Igneous Province: extent and characteristics based on new $^{40}\text{Ar}/^{39}\text{Ar}$ and geochemical data. *Lithos* 110, 294–304.
- Floyd, P.A., Kelling, G., Gökçen, S.L., Gökçen, N., 1991. Geochemistry and tectonic environment of basaltic rocks from the Misis ophiolitic mélange, south Turkey. *Chemical Geology* 89, 263–280.
- Gaetani, M., Garzanti, E., 1991. Multicyclic history of the northern India continental margin (northwestern Himalaya). *American Association of Petroleum Geologists Bulletin* 75, 1427–1446.
- Garzanti, E., Casnedi, R., Jadoul, F., 1986. Sedimentary evidence of a Cambro–Ordovician orogenic event in the northwestern Himalaya. *Sedimentary Geology* 48, 237–265.
- Gehrels, G.E., DeCelles, P.G., Martin, A., Ojha, T.P., Pinhasi, G., Upreti, B.N., 2003. Initiation of the Himalayan Orogen as an early Paleozoic thin-skinned thrust belt. *GSA Today* 13, 4–9.
- Gehrels, G.E., DeCelles, P.G., Ojha, T.P., Upreti, B.N., 2006. Geologic and U–Th–Pb geochronologic evidence for early Paleozoic tectonism in the Kathmandu thrust sheet, central Nepal Himalaya. *Geological Society of America Bulletin* 118, 185–198.
- Genç, Ş.C., Tüysüz, O., 2010. Tectonic setting of the Jurassic bimodal magmatism in the Sakarya Zone (Central and Western Pontides), northern Turkey: a geochemical and isotopic approach. *Lithos* 118, 95–111.
- Glass, L.M., Phillips, D., 2006. The Kalkarindji Continental Flood Basalt Province: a new Large Igneous Province in Australia with possible links to end-Early Cambrian faunal extinctions. *Geology* 34, 461–464.
- Gorton, M.P., Schandl, E.S., 2000. From continents to island arcs: a geochemical index of tectonic setting for arc-related and within-plate felsic to intermediate volcanic rocks. *The Canadian Mineralogist* 38, 1065–1073.
- Griffin, W.L., Pearson, N.J., Belousova, E., Jackson, S.E., van Acherbergh, E., O'Reilly, S.Y., Shee, S.R., 2000. The Hf isotope composition of cratonic mantle: LAM–MC–ICPMS analysis of zircon megacrysts in kimberlites. *Geochimica et Cosmochimica Acta* 64, 133–147.
- Griffin, W.L., Wang, X., Jackson, S.E., Pearson, N.J., O'Reilly, S.Y., Xu, X., Zhou, X., 2002. Zircon chemistry and magma mixing, SE China: in-situ analysis of Hf isotopes, Tonglu and Pingtan igneous complexes. *Lithos* 61, 237–269.
- Gürsu, S., Göncüoğlu, M.C., 2005. Early Cambrian back-arc volcanism in the western Taurides, Turkey: implications for rifting along the northern Gondwanan margin. *Geological Magazine* 142, 617–631.
- Guynn, J.H., Kapp, P., Pullen, A., Gehrels, G., Heizler, M., Ding, L., 2006. Tibetan basement rocks near Amdo reveal “missing” Mesozoic tectonism along the Bangong suture, central Tibet. *Geology* 34, 505–508.
- Guynn, J., Kapp, P., Gehrels, G., Ding, L., 2012. U–Pb geochronology of basement rocks in central Tibet and paleogeographic implications. *Journal of Asian Earth Sciences*. doi:10.1016/j.jseas.2011.09.003.
- Hanley, L.M., Wingate, M.T.D., 2000. SHRIMP zircon age for an Early Cambrian dolerite dyke: an intrusive phase of the Antrim Plateau Volcanics of northern Australia. *Australian Journal of Earth Sciences* 47, 1029–1040.
- Hassanzadeh, J., Stockli, D.F., Horton, B.K., Axen, G.J., Stockli, L.D., Grove, M., Schmitt, A., Walker, J.D., 2008. U–Pb zircon geochronology of upper Neoproterozoic–Early Cambrian granitoids in Iran: implications for paleogeography, metallogeny, and exhumation history of Iranian basement. *Tectonophysics* 451, 71–96.
- Hastie, A.R., Kerr, A.C., Pearce, J.A., Mitchell, S.F., 2007. Classification of altered volcanic island arc rocks using immobile trace elements: development of the Th–Co discrimination diagram. *Journal of Petrology* 48, 2341–2357.
- He, S.D., Kapp, P., DeCelles, P.G., Gehrels, G.E., Heizler, M., 2007. Cretaceous–Tertiary geology of the Gangdese Arc in the Linzhou area, southern Tibet. *Tectonophysics* 433, 15–37.
- Hickey, R.L., Frey, F.A., Gerlach, C., 1986. Multiple sources for basaltic arc rocks from the southern zone of the Andes: trace element and isotopic evidence for contributions from subducted oceanic crust, mantle, and continental crust. *Journal of Geophysical Research* 91, 5963–5983.
- Hildreth, W., Halliday, A.N., Christiansen, R.L., 1991. Isotopic and chemical evidence concerning the genesis and contamination of basaltic and rhyolitic magma beneath the Yellowstone plateau volcanic field. *Journal of Petrology* 32, 63–138.
- Hocking, R.M., Mory, A.J., 2006. Geology of the Kalbarri area – a field guide. Western Australia Geological Survey. Record 2006 (19), 1–15.
- Horton, B.K., Hassanzadeh, J., Stockli, D.F., Axen, G.J., Gillis, R.J., Guest, B., Amiri, A.H., Fakhari, M., Zamanzadeh, S.M., Grove, M., 2008. Detrital zircon provenance of Neoproterozoic to Cenozoic deposits in Iran: implications for chronostratigraphy and collisional tectonics. *Tectonophysics* 451, 97–122.
- Hoskin, P.W.O., Schaltegger, U., 2003. The composition of zircon and igneous and metamorphic petrogenesis. In: Manchar, J.M., Hoskin, P.W.O. (Eds.), *Zircon: Reviews of Mineralogy and Geochemistry*, 53, pp. 27–62.
- Huang, Y., Deng, G.B., Peng, C.L., Hao, J.X., Zhang, G.X., 2009. The discovery and significance of absence in Early–Middle Ordovician in southern Baoshan, western Yunnan. *Guizhou Geology* 26, 1–6 (in Chinese with English abstract).
- Ikedai, Y., Yuasa, M., 1989. Volcanism in nascent back-arc basins behind the Schichito Ridge and adjacent areas in the Izu–Ogasawara arc, NW Pacific: evidence for mixing between E-type MORB and island arc magmas at the initiation of back-arc rifting. *Contributions to Mineralogy and Petrology* 101, 377–393.
- Jackson, S.E., Pearson, N.J., Griffin, W.L., Belousova, E.A., 2004. The application of laser ablation–inductively coupled plasma–mass spectrometry to in situ U–Pb zircon geochronology. *Chemical Geology* 211, 47–69.
- Ji, W.H., Chen, S.J., Zhao, Z.M., Li, R.S., He, S.P., Wang, C., 2009a. Discovery of the Cambrian volcanic rocks in the Xainza area, Gangdese orogenic belt, Tibet, China and its significance. *Geological Bulletin of China* 9, 1350–1354 (in Chinese with English abstract).
- Ji, W.Q., Wu, F.Y., Chung, S.L., Li, J.X., Liu, C.Z., 2009b. Zircon U–Pb chronology and Hf isotopic constraints on the petrogenesis of Gangdese batholiths, southern Tibet. *Chemical Geology* 262, 229–245.
- Jolly, W.T., Lidiak, E.G., Dickin, A.P., 2008. Bimodal volcanism in northeast Puerto Rico and the Virgin Islands (Greater Antilles Island Arc): genetic links with Cretaceous subduction of the mid-Atlantic ridge Caribbean spur. *Lithos* 103, 393–414.
- Jones, D.S., Barnes, C.G., Premo, W.R., Snoko, A.W., 2011. The geochemistry and petrogenesis of the Paleoproterozoic Green Mountain arc: a composite(?), bimodal, oceanic, fringing arc. *Precambrian Research* 185, 231–249.
- Kapp, P., Murphy, M.A., Yin, A., Harrison, T.M., Ding, L., Guo, J.R., 2003. Mesozoic and Cenozoic tectonic evolution of the Shiquanhe area of western Tibet. *Tectonics* 22, 1029. doi:10.1029/2001TC001332.
- Kapp, J.L.D., Harrison, T.M., Kapp, P., Grove, M., Lovera, O.M., Ding, L., 2005a. Nyainqentanglha Shan: a window into the tectonic, thermal, and geochemical evolution of the Lhasa block, southern Tibet. *Journal of Geophysical Research* 110, B08413. doi:10.1029/2004JB003330.
- Kapp, P., Yin, A., Harrison, T.M., Ding, L., 2005b. Cretaceous–Tertiary shortening, basin development, and volcanism in central Tibet. *Geological Society of America Bulletin* 117, 865–878.
- Kapp, P., DeCelles, P.G., Gehrels, G.E., Heizler, M., Ding, L., 2007. Geological records of the Lhasa–Qiangtang and Indo–Asian collisions in the Nima area of central Tibet. *Geological Society of America Bulletin* 119, 917–932.
- Kay, R.W., Kay, S.M., 1993. Delamination and delamination magmatism. *Tectonophysics* 219, 177–189.
- Kemp, A.I.S., Hawkesworth, C.J., 2006. Using hafnium and oxygen isotopes in zircons to unravel the record of crustal evolution. *Chemical Geology* 226, 144–162.
- Kemp, A.I.S., Hawkesworth, C.J., Foster, G.L., Paterson, B.A., Woodhead, J.D., Hergt, J.M., Gray, C.M., Whitehouse, M.J., 2007. Magmatic and crustal differentiation history of granitic rocks from Hf–O isotopes in zircon. *Science* 16, 980–983.
- Keto, L.S., Jacobsen, S.B., 1987. Nd and Sr isotopic variations of Early Paleozoic oceans. *Earth and Planetary Science Letters* 84, 27–41.
- Kusky, T.M., Abdelsalam, M., Stern, R.J., Tucker, R.D., 2003. Evolution of the East African and related orogens, and the assembly of Gondwana. *Precambrian Research* 123, 81–85.
- La Flèche, R., Camiré, G., Jenner, G.A., 1998. Geochemistry of post-Adriatic, Carboniferous continental intraplate basalts from the Maritimes Basin, Magdalen islands, Québec, Canada. *Chemical Geology* 148, 115–136.
- Le Fort, P., Debon, F., Pêcher, A., Sonet, J., Vidal, P., 1986. The 500 Ma magmatic event in Alpine southern Asia: a thermal episode at Gondwana scale. *Sciences de la Terre, Mémoires (Nancy)* 47, 191–209.
- Lee, J., Whitehouse, M.J., 2007. Onset of mid-crustal extensional flow in southern Tibet: evidence from U/Pb zircon ages. *Geology* 35, 45–48.
- Li, X.H., Li, W.X., Li, Z.X., Liu, Y., 2008a. 850–790 Ma bimodal volcanic and intrusive rocks in northern Zhejiang, South China: a major episode of continental rift magmatism during the breakup of Rodinia. *Lithos* 102, 341–357.
- Li, Z.X., Bogdanova, S.V., Collins, A.S., Davidson, A., Waele, B. De, Ernst, R.E., Fitzsimons, I.C.W., Fuck, R.A., Gladkochub, D.P., Jacobs, J., Karlstrom, K.E., Lu, S., Natapov, L.M., Pease, V., Pisarevsky, S.A., Thrane, K., Vernikovsky, V., 2008b. Assembly, configuration, and break-up history of Rodinia: a synthesis. *Precambrian Research* 160, 179–210.
- Li, X.H., Li, W.X., Li, Z.X., Lo, C.H., Wang, J., Ye, M.F., Yang, Y.H., 2009. Amalgamation between the Yangtze and Cathaysia Blocks in South China: constraints from SHRIMP U–Pb zircon ages, geochemistry and Nd–Hf isotopes of the Shuangxiwu volcanic rocks. *Precambrian Research* 174, 117–128.
- Li, C., Wu, Y.W., Wang, M., Yang, H.T., 2010. Significant progress on Pan-African and Early Paleozoic orogenic events in Qinghai–Tibet Plateau: discovery of Pan-African orogenic unconformity and Cambrian System in the Gangdese area, Tibet, China. *Geological Bulletin of China* 29, 1733–1736 (in Chinese with English Abstract).
- Lindsay, J.F., Kruse, P.D., Green, O.R., Hawkins, E., Brasier, M.D., Cartlidge, J., Corfield, R.M., 2005. The Neoproterozoic–Cambrian record in Australia: a stable isotope study. *Precambrian Research* 143, 113–133.
- Liu, Y.S., Gao, S., Yuan, H.L., Zhou, L., Liu, X.M., Wang, X.C., Hu, Z.C., Wang, L.S., 2004. U–Pb zircon ages and Nd, Sr, and Pb isotopes of lower crustal xenoliths from North China Craton: insights on evolution of lower continental crust. *Chemical Geology* 211, 87–109.
- Liu, Q.S., Jiang, W., Jian, P., Ye, P.S., Wu, Z.H., Hu, D.G., 2006. The zircon SHRIMP U–Pb age and petrochemical and geochemical features of Mesozoic muscovite monzogranite at Ningzhong, Tibet. *Acta Petrologica Sinica* 22, 643–652 (in Chinese with English abstract).

- Liu, Y.S., Hu, Z.C., Gao, S., Günther, D., Xu, J., Gao, C.G., Chen, H.H., 2008. In situ analysis of major and trace elements of anhydrous minerals by LA-ICP-MS without applying an internal standard. *Chemical Geology* 257, 34–43.
- Liu, S., Hu, R.Z., Gao, S., Feng, C.X., Huang, Z.L., Lai, S.C., Yuan, H.L., Liu, X.M., Coulson, I.M., Feng, G.Y., Wang, T., Qi, Y.Q., 2009. U–Pb zircon, geochemical and Sr–Nd–Hf isotopic constraints on the age and origin of Early Palaeozoic I-type granite from the Tengchong–Baoshan Block, Western Yunnan Province, SW China. *Journal of Asian Earth Sciences* 36, 168–182.
- Liu, Y.S., Gao, S., Hu, Z.C., Gao, C.G., Zong, K.Q., Wang, D.B., 2010a. Continental and oceanic crust recycling-induced melt–peridotite interactions in the Trans-North China Orogen: U–Pb dating, Hf isotopes and trace elements in zircons of mantle xenoliths. *Journal of Petrology* 51, 537–571.
- Liu, Y.S., Hu, Z.C., Zong, K.Q., Gao, C.G., Gao, S., Xu, J., Chen, H.H., 2010b. Reappraisal and refinement of zircon U–Pb isotope and trace element analyses by LA-ICP-MS. *Chinese Science Bulletin* 55, 1535–1546.
- Lu, S.W., Du, F.J., Ren, J.D., Zhang, Y.Q., Liu, P.D., Pei, Z.C., Jia, G.X., Xie, C.Y., Li, X.Z., 2011. 1: 250, 000 geological report of Nyima County with geological map. China University of Geosciences Press, Wuhan, 1–264 (in Chinese).
- Ludwig, K.R., 2003. *Isoplot v. 3.0: a geochronological toolkit for Microsoft Excel*. Berkeley Geochronology Center, Special Publication No. 4, pp. 1–70.
- Macdonald, F.A., Wingate, M.T.D., Mitchell, K., 2005. Geology and age of the Glikson impact structure, Western Australia. *Australian Journal of Earth Sciences* 52, 641–651.
- Mahmoud, R.I., Wali, F.S., František, H.V., Jan, K., Wolfgang, F., 2011. Magmatic and metamorphic evolution of the Shotur Kuh metamorphic complex (Central Iran). *International Journal of Earth Sciences* 100, 45–62.
- Meert, J., 2003. A synopsis of events related to the assembly of eastern Gondwana. *Tectonophysics* 362, 1–40.
- Meert, J.G., Van der Voo, R., 1997. The assembly of Gondwana (800–550 Ma). *Journal of Geodynamics* 23, 223–235.
- Metcalf, I., 1998. Paleozoic and Mesozoic geological evolution of the SE Asian region, multidisciplinary constraints and implications for biogeography. In: Hall, R., Holloway, J.D. (Eds.), *Biogeography and Geological Evolution of SE Asia*. Backhuys Publishers, Amsterdam, pp. 25–41.
- Metcalf, I., 2006. Palaeozoic and Mesozoic tectonic evolution and paleogeography of East Asian crustal fragments: the Korean Peninsula in context. *Gondwana Research* 9, 24–46.
- Metcalf, I., 2009. Late Palaeozoic and Mesozoic tectonic and palaeogeographic evolution of SE Asia. *The Geological Society, London, Special Publications* 315, 7–23.
- Miller, C., Thöni, M., Frank, W., Grasesman, B., Klötzli, U., Gruntli, P., Draganits, E., 2001. The early Palaeozoic magmatic event in the Northwest Himalaya, India: source, tectonic setting and age of emplacement. *Geological Magazine* 138, 237–251.
- Mitchell, A., Chung, S.L., Oo, T., Lin, T.H., Hung, C.H., in press. Zircon U–Pb ages in Myanmar: magmatic–metamorphic events and the closure of a Neo-Tethys Ocean? *Journal of Asian Earth Sciences*.
- Mo, X.X., Niu, Y.L., Dong, G.C., Zhao, Z.D., Hou, Z.Q., Zhou, S., Ke, S., 2008. Contribution of syncollisional felsic magmatism to continental crust growth: a case study of the Paleocene Linzong Volcanic Succession in southern Tibet. *Chemical Geology* 250, 49–67.
- Mory, A.J., Iasky, R.P., Ghori, K.A.R., 2003. A summary of the geological evolution and petroleum potential of the Southern Carnarvon Basin, Western Australia. *Western Australia Geological Survey, Report* 86, 1–26.
- Murphy, J.B., Nance, R.D., 1991. Supercontinent model for the contrasting character of Late Proterozoic orogenic belts. *Geology* 19, 469–472.
- Murphy, J.B., van Staal, C.R., Collins, W.J., 2011. A comparison of the evolution of arc complexes in Paleozoic interior and peripheral orogens: speculations on geodynamic correlations. *Gondwana Research* 19, 812–827.
- Myrow, P.M., Thompson, K.R., Hughes, N.C., Paulsen, T.S., Sell, B.K., Parcha, S.K., 2006. Cambrian stratigraphy and depositional history of the northern Indian Himalaya, Spiti Valley, north-central India. *Geological Society of America Bulletin* 118, 491–510.
- Pan, G.T., Ding, J., Yao, D.S., Wang, L.Q., 2004. Guidebook of 1:1500000 geologic map of the Qinghai–Xizang (Tibet) plateau and adjacent areas. Chengdu, China, Chengdu Cartographic Publishing House, 1–48.
- Pan, G.T., Mo, X.X., Hou, Z.Q., Zhu, D.C., Wang, L.Q., Li, G.M., Zhao, Z.D., Geng, Q.R., Liao, Z.L., 2006. Spatial–temporal framework of the Gangdese Orogenic Belt and its evolution. *Acta Petrologica Sinica* 22, 521–533 (in Chinese with English abstract).
- Pearce, J.A., Norry, M.J., 1979. Petrogenetic implications of Ti, Zr, Y, and Nb. Variations in volcanic rocks. *Contributions to Mineralogy and Petrology* 69, 33–37.
- Pearce, J.A., Peate, D.W., 1995. Tectonic implications of the composition of volcanic arc magmas. *Annual Review of Earth and Planetary Sciences* 23, 251–285.
- Pin, C., Paquette, J.L., 1997. A mantle-derived bimodal suite in the Hercynian belt: Nd isotope and trace element evidence for a subduction-related rift origin of the late Devonian Brevenne metavolcanics, Massif Central (France). *Contributions to Mineralogy and Petrology* 123, 222–238.
- Pullen, A., Kapp, P., Gehrels, G.E., Ding, L., Zhang, Q.H., 2011. Metamorphic rocks in central Tibet: lateral variations and implications for crustal structure. *Geological Society of America Bulletin* 123, 585–600.
- Quigley, M.C., Yu, L.J., Gregory, C., Corvino, A., Sandiford, M., Wilson, C.J.L., Liu, X.H., 2008. U–Pb SHRIMP zircon geochronology and T–t–d history of the Kampa Dome, southern Tibet. *Tectonophysics* 446, 97–113.
- Ramezani, J., Tucker, R.D., 2003. The Saghband Region, Central Iran: U–Pb geochronology, petrogenesis and implications for Gondwana tectonics. *American Journal of Science* 303, 622–665.
- Reichow, M.K., Saunders, A.D., White, R.V., Al'Mukhamedov, A.I., Medvedev, A.Ya., 2005. Geochemistry and petrogenesis of basalts from the West Siberian Basin: an extension of the Permo–Triassic Siberian Traps, Russia. *Lithos* 79, 425–452.
- Rollinson, H.R., 1993. *Using Geochemical Data: Evaluation, Presentation, Interpretation*. Longman Group UK Ltd., New York, pp. 1–352.
- Rudnick, R.L., Gao, S., Ling, W.L., Liu, Y.S., McDonough, W.F., 2004. Petrology and geochemistry of spinel peridotite xenoliths from Hannuoba and Qixia, North China craton. *Lithos* 77, 609–637.
- Saki, A., 2010. Proto-Tethyan remnants in northwest Iran: geochemistry of the gneisses and metapelitic rocks. *Gondwana Research* 17, 704–714.
- Saunders, A.D., Tarney, J., 1984. Geochemical characteristics of basaltic volcanism within back-arc basins. In: Kokelaar, B.P., Howells, M.F. (Eds.), *Marginal Basin Geology: Geological Society of London Special Publication*, 16, pp. 59–76.
- Sengör, A.M.C., 1987. Tectonics of the Tethysides: orogenic collage development in a collisional setting. *Annual Review of Earth and Planetary Sciences* 15, 213–244.
- Shellnutt, J.G., Zhou, M.F., 2007. Permian peralkaline, peraluminous and metaluminous A-type granites in the Panxi district, SW China: their relationship to the Emeishan mantle plume. *Chemical Geology* 243, 286–316.
- Shi, C., Li, R.S., He, S.P., Wang, C., Pan, S.J., Liu, Y., Gu, P.Y., 2010. LA-ICP-MS zircon U–Pb dating for gneissic garnet-bearing biotite granodiorite in the Yadong area, southern Tibet, China and its geological significance. *Geological Bulletin of China* 29, 1745–1753 (in Chinese with English abstract).
- Shinjo, R., Chung, S.L., Kato, Y., Kimura, M., 1999. Geochemical and Sr–Nd isotopic characteristics of volcanic rocks from the Okinawa Trough and Ryukyu arc: implications for the evolution of a young, intracontinental back arc basin. *Journal of Geophysical Research* 104, 10591–10608.
- Smith, I.E.M., Worthington, T.J., Price, R.C., Stewart, R.B., Maas, R., 2006. Petrogenesis of dacite in an oceanic subduction environment: Raoul Island, Kermadec Arc. *Journal of Volcanology and Geothermal Research* 156, 252–265.
- Soderlund, U., Patchett, P.J., Vervoort, J.D., Isachsen, C.E., 2004. The ¹⁷⁶Lu decay constant determined by Lu–Hf and U–Pb isotope systematics of Precambrian mafic intrusions. *Earth and Planetary Science Letters* 219, 311–324.
- Song, S.G., Ji, J.Q., Wei, C.J., Su, L., Zheng, Y.D., Song, B., Zhang, L.F., 2007. Early Paleozoic granite in Nujiang River of northwest Yunnan in southwestern China and its tectonic implications. *Chinese Science Bulletin* 52, 2402–2406.
- Song, S.G., Niu, Y.L., Wei, C.J., Ji, J.Q., Su, L., 2010. Metamorphism, anatexis, zircon ages and tectonic evolution of the Gongshan block in the northern Indochina continent – an eastern extension of the Lhasa Block. *Lithos* 120, 327–346.
- Sui, Q.L., Zhu, D.C., Zhao, Z.D., Zhang, X.Q., Wang, Q., Liu, M., Mo, X.X., 2010. Compositional diversity of ca. 110 Ma magmatism in the northern Lhasa subterranean, Tibet: implication for petrogenesis and crustal growth in continent–continent collision zone. *National Conference on Petrology and Geodynamics Abstracts*, Beijing, China, pp. 93–94 (in Chinese).
- Sun, S.S., McDonough, W.F., 1989. Chemical and isotope systematics of oceanic basalts: implications for mantle composition and processes. In: Saunders, A.D. (Ed.), *Magmatism in Ocean Basins: Geological Society Publication*, 42, pp. 313–345.
- Ueno, K., 2003. The Permian fusulinoid faunas of the Sibumasu and Baoshan blocks: their implications for the paleogeographic and paleoclimatologic reconstruction of the Cimmerian Continent. *Palaogeography, Palaeoclimatology, Palaeoecology* 193, 1–24.
- Ustaömer, P.A., Ustaömer, T., Collins, A.S., Robertson, A.H.F., 2009. Cadomian (Ediacaran–Cambrian) arc magmatism in the Bitlis Massif, SE Turkey: magmatism along the developing northern margin of Gondwana. *Tectonophysics* 473, 99–112.
- Wang, X.D., Ueno, K., Mizuno, Y., Sugiyama, T., 2001. Late Paleozoic faunal, climatic and geographic changes in the Baoshan block as a Gondwana-derived continental fragment in Southwest China. *Palaogeography, Palaeoclimatology, Palaeoecology* 170, 197–218.
- Wang, Y.J., Zhang, F.F., Fan, W.M., Zhang, G.W., Chen, S.Y., Cawood, P.A., Zhang, A.M., 2010. Tectonic setting of the South China Block in the early Paleozoic: resolving intracontinental and ocean closure models from detrital zircon U–Pb geochronology. *Tectonics* 29, TC6020. doi:10.1029/2010TC002750.
- Wang, X.X., Zhang, J.J., Yang, X.Y., Zhang, B., 2011. Zircon SHRIMP U–Pb ages, Hf isotopic features and their geological significance of the Greater Himalaya Crystalline Complex augen gneiss in Gyirong area, south Tibet. *Earth Science Frontiers* 18, 127–139 (in Chinese with English abstract).
- Wang, Q., Zhu, D.C., Zhao, Z.D., Guan, Q., Zhang, X.Q., Sui, Q.L., Hu, Z.C., Mo, X.X., 2012. Magmatic zircons from I-, S- and A-type granitoids in Tibet: trace element characteristics and their application to detrital zircon provenance study. *Journal of Asian Earth Sciences*. doi:10.1016/j.jseaes.2011.07.027.
- Whalen, J.B., Currie, K.L., Chappell, B.W., 1987. A-type granites: geochemical characteristics, discrimination and petrogenesis. *Contributions to Mineralogy and Petrology* 95, 407–419.
- Winchester, J.A., Floyd, P.A., 1977. Geochemical discrimination of different magma series and their differentiation products using immobile elements. *Chemical Geology* 20, 325–343.
- Xiao, L., Xu, Y.G., Mei, H.J., Zheng, Y.F., He, B., Pirajno, F., 2004. Distinct mantle sources of low-Ti and high-Ti basalts from the western Emeishan large igneous province, SW China: implications for plume–lithosphere interaction. *Earth and Planetary Science Letters* 228, 525–546.
- Xie, C.M., Li, C., Su, L., Wu, Y.W., Wang, M., Yu, H., 2010. LA-ICPMS U–Pb dating of zircon from granite–gneiss in the Amdo area, northern Tibet, China. *Geological Bulletin of China* 29, 1737–1744 (in Chinese with English abstract).
- Xu, R.H., Schärer, U., Allègre, C.J., 1985. Magmatism and metamorphism in the Lhasa block (Tibet): a geochronological study. *Journal of Geology* 93, 41–57.
- Yang, J.H., Wu, F.Y., Wilde, S.A., Xie, L.W., Yang, Y.H., Liu, X.M., 2007. Tracing magma mixing in granite genesis: in situ U–Pb dating and Hf-isotope analysis of zircons. *Contributions to Mineralogy and Petrology* 153, 177–190.
- Yin, A., Harrison, T.M., 2000. Geologic evolution of the Himalayan–Tibetan orogen. *Annual Review of Earth and Planetary Sciences* 28, 211–280.

- Yuan, H.L., Gao, S., Dai, M.N., Zong, C.L., Günther, D., Fontaine, G.H., Liu, X.M., Diwu, C.R., 2008. Simultaneous determinations of U–Pb age, Hf isotopes and trace element compositions of zircon by excimer laser ablation quadrupole and multiple collector ICP-MS. *Chemical Geology* 247, 100–118.
- Zhang, X.H., Zhang, H.F., Tang, Y.J., Wilde, S.A., 2008a. Geochemistry of Permian bimodal volcanic rocks from central Inner Mongolia, North China: implication for tectonic setting and Phanerozoic continental growth in Central Asian Orogenic belt. *Chemical Geology* 249, 262–281.
- Zhang, Z.M., Wang, J.L., Shen, K., Shi, C., 2008b. Paleozoic circum-Gondwana orogens: petrology and geochronology of the Namche Barwa Complex in the eastern Himalayan syntaxis, Tibet. *Acta Petrologica Sinica* 24, 1627–1637 (in Chinese with English abstract).
- Zhang, Z.M., Dong, X., Geng, G.S., Wang, W., Yu, F., Liu, F., 2010. Precambrian metamorphism of the northern Lhasa Terrane, south Tibet and its tectonic implications. *Acta Geologica Sinica* 84, 449–456 (in Chinese with English abstract).
- Zhang, X.H., Mao, Q., Zhang, H.F., Zhai, M.G., Yang, Y.H., Hu, Z.C., 2011. Mafic and felsic magma interaction during the construction of high-K calc-alkaline plutons within a metacratonic passive margin: the Early Permian Guyang batholith from the northern North China Craton. *Lithos* 125, 569–591.
- Zhao, J.H., Zhou, M.F., Yan, D.P., Zheng, J.P., Li, J.W., 2011. Reappraisal of the ages of Neoproterozoic strata in South China: no connection with the Grenvillian orogeny. *Geology* 39, 299–302.
- Zhu, D.C., Pan, G.T., Mo, X.X., Liao, Z.L., Jiang, X.S., Wang, L.Q., Zhao, Z.D., 2007. Petrogenesis of volcanic rocks in the Sangxiu Formation, central segment of Tethyan Himalaya: a probable example of plume–lithosphere interaction. *Journal of Asian Earth Sciences* 29, 320–335.
- Zhu, D.C., Mo, X.X., Niu, Y.L., Zhao, Z.D., Wang, L.Q., Liu, Y.S., Wu, F.Y., 2009a. Geochemical investigation of Early Cretaceous igneous rocks along an east–west traverse throughout the central Lhasa Terrane, Tibet. *Chemical Geology* 268, 298–312.
- Zhu, D.C., Mo, X.X., Niu, Y.L., Zhao, Z.D., Wang, L.Q., Pan, G.T., Wu, F.Y., 2009b. Zircon U–Pb dating and in-situ Hf isotopic analysis of Permian peraluminous granite in the Lhasa terrane, southern Tibet: implications for Permian collisional orogeny and paleogeography. *Tectonophysics* 469, 48–60.
- Zhu, D.C., Mo, X.X., Zhao, Z.D., Niu, Y.L., Wang, L.Q., Chu, Q.H., Pan, G.T., Xu, J.F., Zhou, C.Y., 2010. Presence of Permian extension- and arc- type magmatism in southern Tibet: paleogeographic implications. *GSA Bulletin* 122, 979–993.
- Zhu, D.C., Zhao, Z.D., Niu, Y.L., Dilek, Y., Mo, X.X., 2011a. Lhasa Terrane in southern Tibet came from Australia. *Geology* 39, 727–730.
- Zhu, D.C., Zhao, Z.D., Niu, Y.L., Mo, X.X., Chung, S.L., Hou, Z.Q., Wang, L.Q., Wu, F.Y., 2011b. The Lhasa Terrane: record of a microcontinent and its histories of drift and growth. *Earth and Planetary Science Letters* 301, 241–255.
- Zhu, D.C., Zhao, Z.D., Niu, Y.L., Dilek, Y., Hou, Z.Q., Mo, X.X., 2012. The origin and pre-Cenozoic evolution of the Tibetan Plateau. *Gondwana Research*. doi:10.1016/j.gr.2012.02.002.